Chemical Engineering Journal 451 (2023) 138883

Contents lists available at ScienceDirect

Chemical Engineering Journal

journal homepage: www.elsevier.com/locate/cej

Gradational anionic redox enabling high-energy P2-type Na-layered oxide cathode

Seokjin Lee [a,b,1], Wonseok Ko [a,b,1], Hyunyoung Park [a,b], Yongseok Lee [a,b], Jungmin Kang [a,b], Jinho Ahn [a,b], Sangyeop Lee [a,b], Eunji Sim [c,d], Kyuwook Ihm [d], Kyu-Young Park [e,*], Jongsoon Kim [a,b,*]

[a] Department of Energy Science, Sungkyunkwan University, Suwon 16419, Republic of Korea
[b] SKKU Institute of Energy Science and Technology (SIEST), Sungkyunkwan University, Suwon 16419, Republic of Korea
[c] Department of Smart Fabrication Technology, Sungkyunkwan University, Suwon 16419, Republic of Korea
[d] Pohang Accelerator Laboratory, Pohang 37673, Republic of Korea
[e] Graduate Institute of Ferrous and Energy Materials Technology, Pohang University of Science & Technology (POSTECH), Pohang 37673, Republic of Korea

ARTICLE INFO

Keywords:
Na-ion batteries
Cathode
Anionic redox reaction
Rechargeable batteries
First-principles calculation

ABSTRACT

Anionic-redox-based layered oxide materials are considered promising cathodes for Na-ion batteries because of their high energy densities. However, the anionic redox reaction at high voltage results in structural instability of the layered oxides, leading to not only poor electrochemical properties but also structural degradation after prolonged cycling. Herein, through combined studies using first-principles calculation and various experimental techniques, we investigate the role of the combination of earth-abundant Mn, Fe, and Mg in enabling a stable and gradational anionic redox reaction in a P2-type Na-layered oxide cathode during charge/discharge, resulting in outstanding electrochemical performance. At 10 mA g^{-1}, P2-type $Na_{0.67}[Mg_{0.22}Mn_{0.55}Fe_{0.23}]O_2$ delivers a large specific capacity of ~207 mAh g^{-1}, corresponding to ~0.8 mol Na^+ de/intercalation *via* both cationic and anionic redox reactions. The outstanding cycle performance, well-retained crystal structure, and morphology after prolonged cycling indicate that the anionic redox reaction of O^{2-}/O^- stably occurred in the P2-type $Na_{0.67}[Mg_{0.22}Mn_{0.55}Fe_{0.23}]O_2$ structure despite the charging process in the high-voltage region. Furthermore, the use of earth-abundant Mn, Fe, and Mg is beneficial in terms of the economic feasibility for low-cost and high-energy Na-ion batteries. These intensive investigations provide key knowledge for understanding anionic-redox-based cathode materials with high structural stability for Na-ion batteries.

1. Introduction

The importance of sustainable energy storage systems is ever-increasing in an effort to reduce environmental impacts and address the exhaustion of limited energy resources [1–3]. Li-ion batteries (LIBs) have been widely used in portable electronic devices, electric vehicles (EVs), and large-scale energy storage systems (ESSs) owing to their high energy density and long cycle life [4–6]. However, conventional cathode materials, such as $LiCoO_2$ and $Li[Ni_{1-x-y}Co_xMn_y]O_2$, are greatly reliant on certain transition-metal resources, such as Co and Ni, causing the price of LIBs to be affected by the current political climate [7]. In addition, given the recent rise in lithium prices, concerns about the economic feasibility of LIBs are growing. To prepare for these inevitable factors, researchers have aimed to develop alternative energy sources with low production costs and high energy densities as replacements for LIBs.

Recently, Na-ion batteries (NIBs) have received extensive attention as one of the most promising alternatives to LIBs, owing to their use of earth-abundant Na resources and a monovalent-ion-based reaction chemistry similar to that of LIBs [8]. Various promising cathode active materials for NIBs have been introduced, including layered-type transition-metal oxides ($Na_x[TM]O_2$) ([TM]: transition metal) [9,10], polyanion-type compounds [11,12], and Prussian blue analogues [13,14]. The layered-type $Na_x[TM]O_2$ cathode group has been especially highlighted because of the high reversible specific capacity and power capability based on the fast two-dimensional guest-ion diffusion

* Corresponding authors at: Department of Energy Science, Sungkyunkwan University, Suwon 16419, Republic of Korea (Jongsoon Kim).
E-mail addresses: kypark0922@postech.ac.kr (K.-Y. Park), jongsoonkim@skku.edu (J. Kim).
[1] These authors contributed equally to this work.

https://doi.org/10.1016/j.cej.2022.138883
Received 28 June 2022; Received in revised form 16 August 2022; Accepted 25 August 2022
Available online 29 August 2022

pathways. Unlike LIBs, the layered oxide cathodes of NIBs can drive a battery reaction reversibly using inexpensive 3*d* transition metals, which is incomparably advantageous in terms of production cost. More specifically, P2-type $Na_y[Mn_xFe_{1-x}]O_2$ (P2-$Na_y[Mn_xFe_{1-x}]O_2$) cathode materials composed of earth-abundant elements have been introduced as a superior low-cost and non-toxic cathode. However, most researches on P2-$Na_y[Mn_xFe_{1-x}]O_2$ cathode materials have reported their poor electrochemical performance stemming from structural and chemical instability [15]. For example, Tang and co-workers reported on the poor cycle retention of a P2-$Na_{0.67}[Mn_{0.5}Fe_{0.5}]O_2$ cathode, which exhibited a capacity retention of ~56.9 % after 50 cycles even at a low current density of 20 mA g^{-1} [16]. This undesirable cycle performance was associated with the large volume change from the large Na^+ ionic size (1.02 Å) and Jahn–Teller distortion from the Mn^{3+}/Mn^{4+} redox reaction [17,18]. Moreover, to increase the practical gravimetric capacities of the layered oxide group, several studies on the development of novel cathodes based on an anionic redox reaction (O^{2-}/O^-) were recently reported [19–21]. However, the anionic redox reaction is accompanied by structural instability, disordering, and sluggish kinetics, resulting in poor electrochemical performance as well as structural and morphological degradation after prolonged cycling [19,20]. Therefore, to achieve outstanding power capability and cycle performance of anionic-redox-based P2-$Na_y[Mn_xFe_{1-x}]O_2$ cathode materials, enhancement of the structural stability is needed. Various researches on doping of other TM cations in P2-$Na_y[Mn_xFe_{1-x}]O_2$ were reported to improve the electrochemical properties [22–27]. However, it was known that anionic redox reaction of O^{2-}/O^- in Mn-based layered oxide cathode can be occurred when the following conditions are satisfied [28,29]; (1) oxidation state of Mn^{4+}, (2) existence of Na^+ in the structure even after oxidation to Mn^{4+}. In terms of the doped TM cations in P2-$Na_y[Mn_xFe_{1-x}]O_2$, they can be oxidized during charge and provide the electrons for Na^+ deintercalation, like the Mn and Fe cations. Thus, it is difficult to prepare the anionic-redox-based P2-$Na_y[Mn_xFe_{1-x}]O_2$ through the simple doping of TM cations.

Since the redox inactive Mg ion maintains redox state as +2 regardless of Na^+ de/intercalation process, thus the bonding interaction between Mg cation and O anion is less varied during Na^+ de/intercalation than that of between transition metal (TM) cation and O anion, which implies that existence of Mg cations is capable of suppressing Jahn-Teller distortion of Mn based active materials. Thus, we speculated that the structural and electrochemical stabilities of anionic-redox-based P2-$Na_y[Mn_xFe_{1-x}]O_2$ could be successfully enhanced by substitution of a considerably large amount of the Mg^{2+} ions instead of Fe and Mn in [TM] sites. Herein, a novel anionic-redox-based P2-$Na_{0.67}[Mg_{0.22}Mn_{0.55}Fe_{0.23}]O_2$ cathode is shown to exhibit a large specific capacity of ~207 mAh g^{-1} in the voltage range of 1.5–4.4 V (*vs* Na^+/Na) and a stable O^{2-}/O^- redox reaction during prolonged cycling. For 150 cycles at 100 mA g^{-1}, up to ~73 % of the initial capacity was retained with a high coulombic efficiency of > 99 %. Furthermore, after prolonged cycling, the crystal structure and morphologies of P2-$Na_{0.67}[Mg_{0.22}Mn_{0.55}Fe_{0.23}]O_2$ were also well maintained without severe degradation, despite the anionic redox reaction in the high-voltage region. Through combined first-principles calculation and various structural analyses, we revealed that the presence of ~0.22 mol Mg^{2+} ions in [TM] sites can result in the high structural stability of P2-$Na_{0.67}[Mg_{0.22}Mn_{0.55}Fe_{0.23}]O_2$ such as slightly changed local environments of [Mg, Fe, Mn]O_6 octahedra before and after anionic redox reaction by gradationally and selectively oxidizing oxygen anions.

2. Experimental

2.1. Synthesis process of P2-$Na_{0.67}[Mg_{0.22}Mn_{0.55}Fe_{0.23}]O_2$

$Na_{0.67}[Mg_xMn_{0.55}Fe_{0.45-x}]O_2$ (x = 0.11 and 0.22) powder was prepared using the conventional solid-state method. Na_2CO_3 (Sigma Aldrich, 99.5 %), MgO (Sigma Aldrich, 99 %), Mn_2O_3 (Sigma Aldrich, 99 %), and Fe_2O_3 (Samchun, 95 %) were used as precursors. An excess amount of Na_2CO_3 (approximately 5 mol %) was added to compensate for the loss of sodium at high temperatures. Stoichiometric amounts of precursors were mixed using a high-energy ball miller at 400 rpm for 12 h with a mass ratio of 0.9:9.1 of the precursors and silicon–nitride balls. Then, the ball miller was sealed in an Ar-filled glove box to prevent oxygen and water contamination. The homogenous mixed powder was pre-calcined at 450 ℃ for 6 h (heating rate of 2.5 ℃ min^{-1}) under an air atmosphere. The obtained powder was pelletized using a pressure machine under a pressure of 200 kg cm^{-2} and calcined at 900 ℃ for 10 h (heating rate of 2.5 ℃ min^{-1}) under an air atmosphere. After calcination, the sample was cooled to 200 ℃ in the furnace without controlling the cooling rate. And then, the produced sample was rapidly moved into an Ar-filled glove box to avoid contamination by moisture.

2.2. Materials characterization

The crystal structure of $Na_{0.67}[Mg_xMn_{0.55}Fe_{0.45-x}]O_2$ (x = 0.11 and 0.22) was analyzed using XRD (Rigaku, SmartLab) with Cu Kα radiation (λ = 1.54178 Å) in the 2θ range of 10° to 80° with a step size of 0.02°. FullProf software was used to conduct Rietveld refinement [30]. The particle morphology and microstructure of $Na_{0.67}[Mg_{0.22}Mn_{0.55}Fe_{0.23}]O_2$ were observed using field-emission scanning electron microscopy (FE-SEM, HITACH S4700) at the Cooperative Center for Research Facilities (CCRF) at Sungkyunkwan University and field-emission transmission electron microscopy (FE-TEM; JEM-F200) at the National Center for Inter-University Research Facilities (NCIRF) at Seoul National University. The atomic ratio of Na, Mg, Mn, and Fe was determined using inductively coupled plasma atomic emission spectrometry (ICP-AES). The *operando* synchrotron XRD (*o*-SXRD) patterns of $Na_{0.67}[Mg_{0.22}Mn_{0.55}Fe_{0.23}]O_2$ were measured to monitor the structural evolution during charge/discharge at a current density of 30 mA g^{-1} in the voltage range of 1.5–4.4 V (*vs* Na^+/Na). The *operando* SXRD patterns of $Na_{0.67}[Mg_{0.22}Mn_{0.55}Fe_{0.23}]O_2$ were obtained at the 3D XRS beamline at Pohang Accelerator Laboratory (PAL), Pohang, South Korea, using synchrotron radiation (λ = 0.688725 Å) in the 2θ range of 13° to 60° with a Mar345 image plate detector in transmission mode and an X-ray exposure time of 5 s. After the measurement, the 2θ angles of all the (*o*-SXRD) patterns were converted into the corresponding angles for λ = 1.54178 Å (the wavelength of a conventional X-ray tube source with Cu Kα radiation) for ease of comparison with other studies. The valence states of Mn and Fe elements in the $Na_{0.67}[Mg_{0.22}Mn_{0.55}Fe_{0.23}]O_2$ structure were measured using the *ex-situ* X-ray absorption spectroscopy (XAS) spectra at the 10C beam line at Pohang Accelerator Laboratory (PAL), Mn and Fe metal foil were used as reference spectra. Mn K-edge spectra and Fe K-edge spectra were collected in transmission mode using high electron energy (2.5 GeV) with a 200-mA current condition including the X-ray absorption near edge structure (XANES) and extended X-ray absorption fine structure (EXAFS) regions. Mn and Fe metal foils were placed in front of the third ionization chamber as an internal reference for energy calibration. The normalized XAS spectra was calibrated using linear regression to fit the pre-edge region and a quadratic polynomial to the post-edge region in the Athena program using metal foil spectra. The valence state of the O element was also measured in total fluorescence yield (TFY) mode using soft X-ray absorption spectroscopy (sXAS) spectra with high-energy grating (HEG) at the 4D PES beamline at Pohang Accelerator Laboratory (PAL). These measured Mn, Fe K-edge XANES, EXAFS, and O K-edge sXAS spectra were analyzed using Athena and Artemis software [31]. For Fourier transform *ex-situ* extended X-ray absorption fine structure (FT-EXAFS) analysis, a radial distribution function with k^3-weight conditions in the fitting range of 1.0–2.0 Å for the first shell corresponding to the TM–O bond was used. At this time, the amplitude reduction factor (S_0^2) is 1.0. These electrode samples were obtained in an Ar-filled glove box with different charge/discharge states (OCV, 4.2 V, 4.4 V, 2.6 V, and 1.5 V) and sealed with Kapton tape. To analyze the chemical bonding, X-ray

photoelectron spectroscopy (XPS) measurements were performed using an AXIS SUPRA (Kratos Analytical) spectrometer with a monochromatic Al Kα (1486.7 eV). For XPS fitting, we used the XPSPEAK41 software and all the XPS spectra were calibrated to the C1*s* peak at a binding energy (BE) of 284.6 eV. The XPS peak deconvoluted into four, which are M−O crystalline network (529.8 eV), $(CO_3)^{2-}$, C═O (531.5 eV), C—O (533 eV), and O^- (530.5 eV).

2.3. Electrochemical characterization

A $Na_{0.67}[Mg_{0.22}Mn_{0.55}Fe_{0.23}]O_2$ electrode was fabricated by mixing active materials (70 wt%), Super P (20 wt% carbon black), and poly (vinylidene fluoride) (10 wt%, PVDF) binder using *N*-methyl-2-pyrrolidone (NMP) as a solvent. The obtained slurry was cast on Al foil using a doctor blade and dried in a vacuum oven at 100 ℃ for 12 h. The final active mass loading of the electrode was ~2 mg cm^{-2}. The $Na_{0.67}[Mg_{0.22}Mn_{0.55}Fe_{0.23}]O_2$ electrode was electrochemically tested using CR2032-type coin cells that were assembled as half-cells using Na metal as a reference/counter electrode, a separator (Whatman GF/F glass fiber), and an electrolyte (1 M $NaPF_6$ in propylene carbonate (PC) and fluoroethylene carbonate (FEC) in a volume ratio of 98:2) in an Ar-filled glove box in the NIB system. Galvanostatic charge/discharge tests were performed at various current densities (10, 15, 30, 60, 100, and 200 mA g^{-1} in the voltage range of 1.5–4.4 V (*vs* Na^+/Na)) using a battery charge/discharge test system (WBCS 3000, WonATech). Full cells were fabricated using commercially available hard carbon (Kureha) as the anode material. The hard carbon was heated at 1000 °C for 2 h (heating rate of 2.5 °C min^{-1}) under an Ar atmosphere to remove residual water contamination and the air oxides on the surface of the hard carbon particles. After calcination, the sample was cooled to 200 ℃ in the furnace without controlling the cooling rate. And then, the produced sample was rapidly moved into an Ar-filled glove box to avoid contamination by moisture. The hard carbon electrode was assembled in the same way as the $Na_{0.67}[Mg_{0.22}Mn_{0.55}Fe_{0.23}]O_2$ electrode, except that Cu foil was used. To minimize the irreversibility of the hard carbon, the hard carbon electrode was pre-cycled into the half-cell through direct contact with Na metal in the range of 0.01–2.0 V (*vs* Na^+/Na) at 10 mA g^{-1}. Finally, CR2032-type full-cells were assembled with the $Na_{0.67}[Mg_{0.22}Mn_{0.55}Fe_{0.23}]O_2$ cathode and the pre-cycled hard carbon anode (capacity ratio of negative and positive electrodes of ~1.2) in an Ar-filled glove box and galvanostatic charge/discharge tests were performed in the voltage range of 1.5–4.4 V (*vs* Na^+/Na) at 10 and 100 mA g^{-1}.

2.4. Computational details

All the DFT calculations were performed using the Vienna *Ab initio* Simulation Package (VASP) [32]. The projector-augmented wave (PAW) pseudopotential was used with a plane-wave basis set, as implanted in VASP [33]. Perdew–Burke–Ernzerhof (PBE) parametrization of the generalized gradient approximation (GGA) was used for the exchange–correlation functional [34]. For the DFT calculations, a 5 × 4 × 3 k-point grid was used to calculate a 2 × 3 × 1 supercell structure of $Na_{0.67}[Mg_{0.22}Mn_{0.55}Fe_{0.23}]O_2$. Thus, total 12 elements exist in the transition metal sites in the supercell. In order to match the element ratio of $Na_{0.67}[Mg_{0.22}Mn_{0.55}Fe_{0.23}]O_2$ closely, the numbers of Mg, Mn and Fe in the supercell were determined 3, 6 and 3, respectively, which implies high reliability of the computational results based on the real atomic composition. The supercell is composed of the 1st transition metal (TM) layer of the supercell with 2 Mg, 3 Mn and 1 Fe and the 2nd TM layer with 1 Mg, 3 Mn and 2 Fe. The GGA + *U* method was adopted to address the localization of the d-orbital in Mn and Fe ions, with *U* values of 4.2 and 3.9 eV, respectively, as used in previous studies [35,36]. The Heyd–Scuseria–Ernzerhof (HSE06) hybrid functional was used to calculate the projected density of states (pDOS) of Mn, Fe, and O [37]. An appropriate number of k-points and a kinetic energy cutoff of 500 eV were used in all the calculations. All the structures were optimized until the force in the unit cell converged to within 0.03 eV $Å^{-1}$. Cluster-assisted statistical mechanics (CASM) software was used to generate all the Na^+/vacancy configurations for each composition, followed by full DFT calculations on a maximum of *x* configurations with the lowest electrostatic energy for each composition used to constitute the convex-hull plot of $Na_{0.67}[Mg_{0.22}Mn_{0.55}Fe_{0.23}]O_2$ [38]. Nudged elastic band (NEB) calculations were performed to determine the activation barrier for Na^+ diffusion in the $Na_{0.67}[Mg_{0.22}Mn_{0.55}Fe_{0.23}]O_2$ structure. To perform the calculations, five intermediate images were generated between each Na site [39]. These structures were then calculated using the NEB algorithm with fixed lattice parameters and free internal atomic positions [40].

3. Results and discussion

3.1. Preparation and characterization of P2-$Na_{0.67}[Mg_{0.22}Mn_{0.55}Fe_{0.23}]O_2$

P2-$Na_{0.67}[Mg_{0.22}Mn_{0.55}Fe_{0.23}]O_2$ powder was synthesized *via* a conventional solid-state reaction method. The transmission electron microscopy (TEM, Fig. 1**a**) and field-emission scanning electron microscopy (FE-SEM, **Fig. S1**) images reveal the typical plate particle morphology with ~0.8 μm size on average. Further compositional analysis using energy-dispersive X-ray spectroscopy (EDS) elemental mapping verifies that Na, Mg, Mn, Fe, and O elements were homogeneously distributed in the particle (Fig. 1**a**) and that the corresponding atomic ratio of Na, Mg, Mn, and Fe elements was 0.670:0.212:0.538:0.242, which well-matched with the inductively coupled plasma atomic emission spectroscopy (ICP-AES) result (**Table S1**).

The P2-type layered oxide has two distinguishable layers for Na ions (with 2b and 2d positions) and transition-metal ions (with 2a position). We determined the occupied crystal site of Mg ions by simultaneously applying a theoretical and experimental approach. Fig. 1**b** shows the relative site energies of the Mg^{2+} cation in each transition-metal and sodium layer using a supercell structure of P2-$Na_{0.67}[Mg_{0.22}Mn_{0.55}Fe_{0.23}]O_2$. In this relatively heavy Mg composition (>20 %), the site energy of the Mg^{2+} cation in the transition-metal layer at the 2a position was much lower (by 300 meV) than that of the sodium layer, suggesting that the Mg^{2+} cation is majorly substituted in transition-metal layers. This result differs from the previous reports of low-Mg^{2+}-concentration doping studies that indicated the Mg substitution at the Na site [41,42]. The amount of substitution is highly affected by the thermodynamic stability with respect to host crystal structure characteristics. There is large difference of ionic radii between Mg^{2+} (0.72 Å) and Na^+ (1.02 Å), thus existence of considerable amounts of Mg cations in the Na layers of the layered-type oxide is thermodynamically unfavorable. Through DFT calculation, moreover, we confirmed that existence of Mg cation in the transition metal (TM) layers is more stable than that in the Na layer. Thus, we speculate that this distinct result is most likely due to the relatively high Mg content in our materials, which is also well matched with the previous research [43,44]. In addition, it was reported that the two superlattice peaks located at 27.2° and 28.3° originated from the in-plane Na^+/vacancy ordering in the crystal structures of Mn-based layered oxide cathodes, which can lower Na-ion diffusion during redox reaction [45,46]. On the other hand, these superlattice were not observed in the XRD pattern of P2-$Na_{0.67}[Mg_{0.22}Mn_{0.55}Fe_{0.23}]O_2$, which implies that the in-plane Na^+/vacancy ordering was suppressed by mixing of Mg, Mn and Fe cations in the TM site. Thus, we supposed that the P2-$Na_{0.67}[Mg_{0.22}Mn_{0.55}Fe_{0.23}]O_2$ structure without the Na^+/vacancy ordering can deliver thermodynamic stability and facile Na^+ diffusion, which results in the stable electrochemical performances of P2-$Na_{0.67}[Mg_{0.22}Mn_{0.55}Fe_{0.23}]O_2$ during Na^+ de/intercalation. The crystal structural analysis based on X-ray diffraction (XRD) pattern and Rietveld refinement was also supportive of

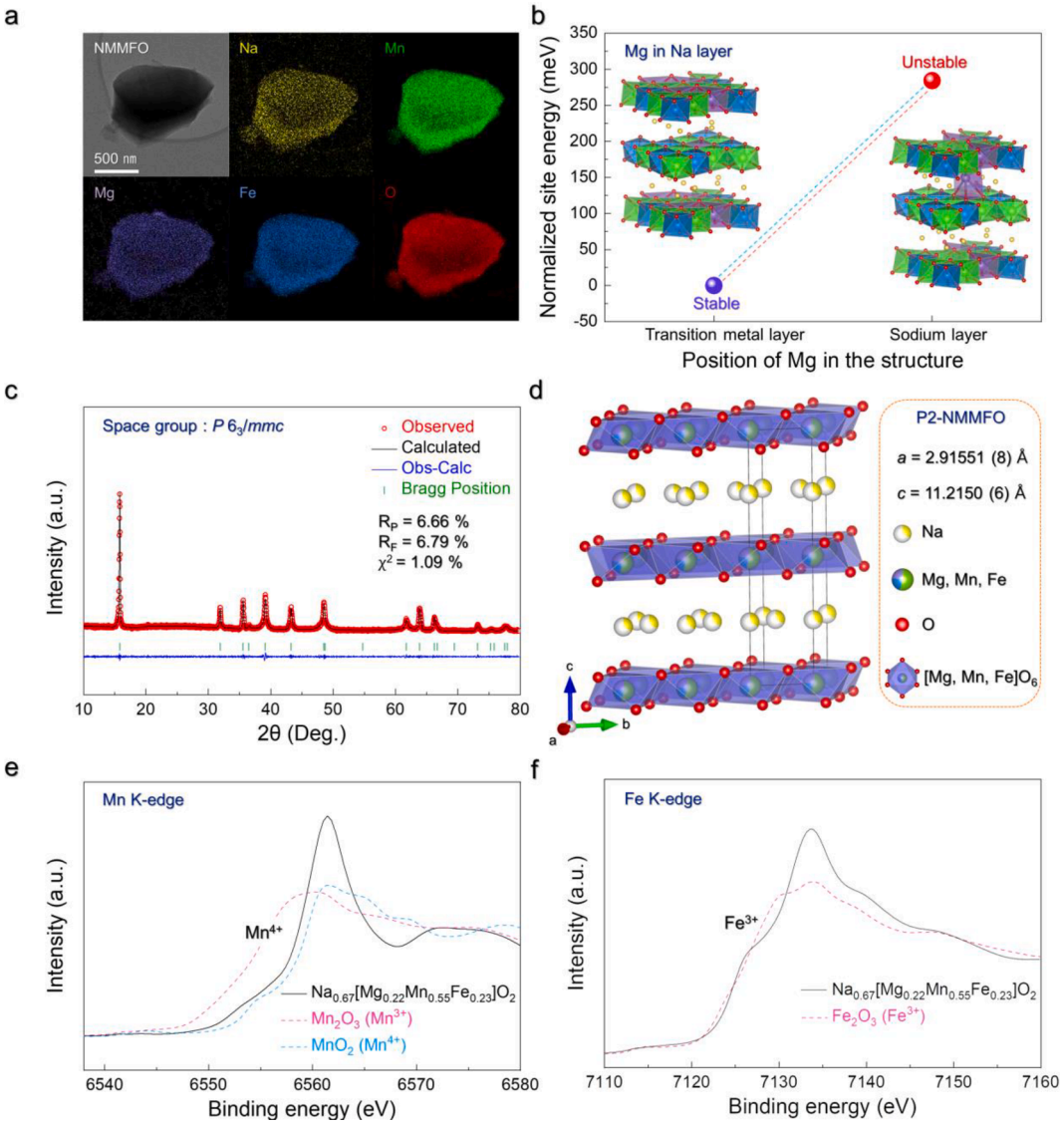

Fig. 1. (a) TEM image and EDS mapping of Na, Mn, Mg, Fe, and O elements of synthesized $Na_{0.67}[Mg_{0.22}Mn_{0.55}Fe_{0.23}]O_2$. (b) Relative site energy of Mg in transition-metal and sodium sites. (c) Rietveld refinement of XRD pattern and (d) corresponding crystal structure of $Na_{0.67}[Mg_{0.22}Mn_{0.55}Fe_{0.23}]O_2$. (e) Mn and (f) Fe K-edge of P2-type $Na_{0.67}[Mg_{0.22}Mn_{0.55}Fe_{0.23}]O_2$ pristine electrode.

the P2-$Na_{0.67}[Mg_{0.22}Mn_{0.55}Fe_{0.23}]O_2$ structure. As shown in Fig. 1**c**, the XRD pattern is well-indexed to the hexagonal structure with *P* 6_3*/mmc* space group with Mg cation at the 2a site. The obtained lattice parameters were $a = b = 2.91551(8)$ Å and $c = 11.2150(6)$ Å. The detailed structural information of P2-$Na_{0.67}[Mg_{0.22}Mn_{0.55}Fe_{0.23}]O_2$, such as the atomic positions, thermal factor (B_{iso}), and occupancy, is summarized in **Table S2**. Especially, it was confirmed through the refinement that all of Mg cations exist in the TM sites, not the Na sites. The low values of reliability factors indicate the high accuracy of our Rietveld refinement work ($R_P = 6.66$ %, $R_I = 8.43$ %, $R_F = 6.79$ %, $\chi^2 = 1.09$ %). Based on these observations, we would like to claim that the heavy Mg cation substitution happens within the TM layers rather than the Na layers. The crystal structure of P2-$Na_{0.67}[Mg_{0.22}Mn_{0.55}Fe_{0.23}]O_2$ consists of edge-shared [Mg, Mn, Fe]O_6 octahedra and Na layers forming an ABBA oxygen stacking sequence (see Fig. 1**d**). The average oxidation states of Mn and Fe were confirmed to be Fe^{3+} and Mn^{4+} in the P2-$Na_{0.67}[Mg_{0.22}Mn_{0.55}Fe_{0.23}]O_2$ structure. The Mn K-edge spectra indicated that the average oxidation state of Mn was close to that of MnO_2 (Mn^{4+}) and that the oxidation state of Fe was identical to that of the Fe_2O_3 (Fe^{3+}) reference (Fig. 1**e and f**) according to X-ray absorption near edge structure (XANES) analyses.

3.2. *Detailed reaction mechanism in P2-$Na_{0.67}[Mg_{0.22}Mn_{0.55}Fe_{0.23}]O_2$ during Na^+ de/intercalation*

The redox-active mechanism of P2-$Na_{0.67}[Mg_{0.22}Mn_{0.55}Fe_{0.23}]O_2$ was investigated using combined theoretical and experimental approaches during Na^+ de/intercalation. The various Na^+/vacancies configurations of $Na_{1-x}[Mg_{0.22}Mn_{0.55}Fe_{0.23}]O_2$ phases ($0 \leq x \leq 1$) was prepared using cluster-assisted statistical mechanisms (CASM) software [38]. Fig. 2**a** shows the convex-hull plot on the relative formation energies of various $Na_x[Mg_{0.22}Mn_{0.55}Fe_{0.23}]O_2$ phases using the real formation energies of $Na_0[Mg_{0.22}Mn_{0.55}Fe_{0.23}]O_2$ and $Na_1[Mg_{0.22}Mn_{0.55}Fe_{0.23}]O_2$ compositions as reference. **Fig. S2** shows the real formation energies of $Na_{1-x}[Mg_{0.22}Mn_{0.55}Fe_{0.23}]O_2$ ($0 \leq x \leq 1$). The convex-hull plot shows not only existence of stable intermittent phases between end compositions but also energy difference between two phases relating to redox potentials, compared to the original plot based on the real formation energies. Thus, the convex hull plot was applied for arranging the formation energies on various compositions of cathode materials with different Na contents and calculating theoretical redox potentials. The relative formation energy was derived using the following equation (1):

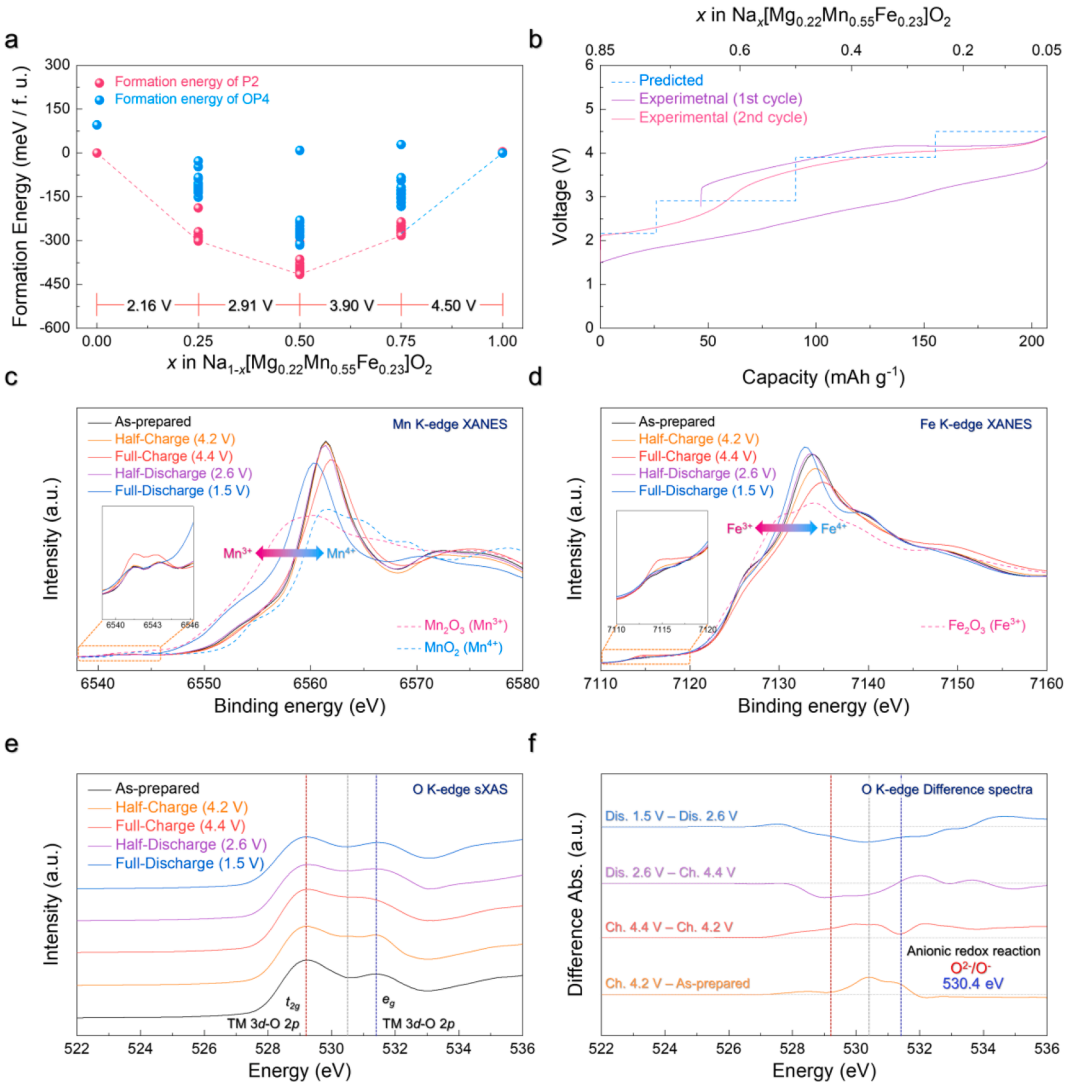

Fig. 2. (a) Convex-hull plot for formation energy of $Na_{1-x}[Mg_{0.22}Mn_{0.55}Fe_{0.23}]O_2$ configurations ($0 \leq x \leq 1$) with theoretical voltage. (b) Comparison of theoretical voltage prediction of $Na_{0.67}[Mg_{0.22}Mn_{0.55}Fe_{0.23}]O_2$ and its experimentally measured charge/discharge profiles. *Ex-situ* (c) Mn and (d) Fe K-edge XANES spectra of various charge/discharge state of $Na_{0.67}[Mg_{0.22}Mn_{0.55}Fe_{0.23}]O_2$. (e) O K-edge sXAS spectra of $Na_x[Mg_{0.22}Mn_{0.55}Fe_{0.23}]O_2$ using total fluorescence yield (TFY) mode. (f) O K-edge difference spectra obtained by subtracting *ex-situ* O K-edge spectra.

$$E_{for} = E(\mathrm{Na}_x[\mathrm{Mg}_{0.22}\mathrm{Mn}_{0.55}\mathrm{Fe}_{0.23}]\mathrm{O}_2) - \frac{(1-x)E(\mathrm{Na}_0[\mathrm{Mg}_{0.22}\mathrm{Mn}_{0.55}\mathrm{Fe}_{0.23}]\mathrm{O}_2) + xE(\mathrm{Na}_1[\mathrm{Mg}_{0.22}\mathrm{Mn}_{0.55}\mathrm{Fe}_{0.23}]\mathrm{O}_2)}{2} \quad (1)$$

where E_{for} is the formation energy for the most stable configuration of each component. These calculation results indicate that the P2-phase is stably retained at compositional range between $Na_1[Mg_{0.22}Mn_{0.55}Fe_{0.23}]O_2$ and $Na_{0.25}[Mg_{0.22}Mn_{0.55}Fe_{0.23}]O_2$. In case of $Na_0[Mg_{0.22}Mn_{0.55}Fe_{0.23}]O_2$ composition, difference of the formation energies between the P2- and OP4-phases is just ~4.6 meV f.u.$^{-1}$, which implies the possibility of coexistence of OP4 and P2 phases even after full Na^+ deintercalation from the structure. The theoretical redox potentials of $Na_{1-x}[Mg_{0.22}Mn_{0.55}Fe_{0.23}]O_2$ during Na^+ de/intercalation were calculated using the following equation (2):

$$V = -\frac{E[Na_{x_2}Mg_{0.22}Mn_{0.55}Fe_{0.23}O_2] - E[Na_{x_1}Mg_{0.22}Mn_{0.55}Fe_{0.23}O_2] - (x_2 - x_1)E[Na]}{(x_2 - x_1)F} \quad (2)$$

where V means the average redox potential depending on the Na–ion content in $Na_{1-x}[Mg_{0.22}Mn_{0.55}Fe_{0.23}]O_2$ ($x_1 \leq x \leq x_2$), E[Na] is the Na metal energy, and F is the Faraday constant. Fig. 2**b** compares the predicted equilibrium potential upon desodiation obtained by the cluster expansion and experimentally measured charge/discharge profile. The corresponding predicted operating voltage was consistent with the actual experimental results, as shown in Fig. 2**b**. Moreover, the initial charge capacity from $Na_{0.67}[Mg_{0.22}Mn_{0.55}Fe_{0.23}]O_2$ resulted in a specific capacity of ~161 mAh g^{-1} at 10 mA g^{-1}. Subsequence discharge down to 1.5 V delivered a larger specific capacity of ~207 mAh g^{-1}, corresponding to intercalation of ~0.8 mol Na^+. In subsequent cycles, ~0.8 mol Na^+ are reversibly deintercalated and intercalated at the structure. As presented in **Fig. S3**, we implemented the differential capacity (dQ/dV) analyses to support the redox reaction mechanism and the stability of oxygen anionic redox reaction during electrochemical cycling with a current density of 100 mA g^{-1}. During initial charge, the dQ/dV was affected by Fe^{3+}/Fe^{4+}-based redox reaction. Then, the anionic redox reaction of O^{2-}/O^- was clearly detected during further charging to 4.4 V (*vs* Na^+/Na). Moreover, three peaks are observed in the dQ/dV curve during discharging to 1.5 V (*vs* Na^+/Na), which indicates the sequential occurrence of O^{2-}/O^-, Fe^{3+}/Fe^{4+}, and Mn^{3+}/Mn^{4+} redox reactions during Na^+ intercalation to $Na_x[Mg_{0.22}Mn_{0.55}Fe_{0.23}]O_2$. After the first cycle, a new peak located at ~2.26 V was observed in the dQ/dV curves, corresponds to the cationic redox reaction of Mn^{3+}/Mn^{4+}. Furthermore, we confirmed that the redox potential on the anionic redox reaction of O^{2-}/O^- was well retained without severe voltage decay during prolonged cycling, which implies the stable occurrence of the anionic redox reaction in $Na_x[Mg_{0.22}Mn_{0.55}Fe_{0.23}]O_2$.

The theoretical calculation suggests the distinguishable cationic and subsequent stable anionic redox reaction. **Fig. S4** shows the integrated spin moments of the Mn, Fe, and O ions as a function of Na content in $Na_x[Mg_{0.22}Mn_{0.55}Fe_{0.23}]O_2$ ($x = 0$, 0.25, 0.5, 0.75, and 1). To clarify the reaction mechanism on Mn^{3+}/Mn^{4+}, Fe^{3+}/Fe^{4+}, and O^{2-}/O^- redox reactions in detail, we compared the integrated spin moments of Mn, Fe, and O in $Na_x[Mg_{0.22}Mn_{0.55}Fe_{0.23}]O_2$ ($x = 0$, 0.25, 0.5, 0.75, and 1). As shown in Fig. S4**a**, it was verified that the net magnetic moment of Mn cation is decreased from 4 to 3 during Na^+ deintercalation from $Na_1[Mg_{0.22}Mn_{0.55}Fe_{0.23}]O_2$ phase to $Na_{0.75}[Mg_{0.22}Mn_{0.55}Fe_{0.23}]O_2$ phase and then it is retained during further Na^+ deintercalation from $Na_{0.75}[Mg_{0.22}Mn_{0.55}Fe_{0.23}]O_2$ phase. In terms of the net magnetic moment of Fe cation, it is changed from 5 to 4 at the range of $Na_{0.75}[Mg_{0.22}Mn_{0.55}Fe_{0.23}]O_2$ and $Na_{0.5}[Mg_{0.22}Mn_{0.55}Fe_{0.23}]O_2$ phases and there is no change at the other ranges (Fig. S4**b**), which implies that Fe^{3+}/Fe^{4+} redox reaction in $Na_x[Mg_{0.22}Mn_{0.55}Fe_{0.23}]O_2$ is occurred after Mn^{3+}/Mn^{4+} redox reaction. Moreover, it was verified that the net magnetic moment of O anion is gradually increased during Na^+ deintercalation from $Na_{0.5}[Mg_{0.22}Mn_{0.55}Fe_{0.23}]O_2$ phase to $Na_0[Mg_{0.22}Mn_{0.55}Fe_{0.23}]O_2$ phase, meaning the gradational and sequential anionic redox reaction of O^{2-}/O^- (Fig. S4**c**). These first-principles calculation results indicated the sequential occurrence of Mn^{3+}/Mn^{4+}, Fe^{3+}/Fe^{4+}, and O^{2-}/O^- redox reactions. XANES analysis was used to determine the change of the oxidation states of the Mn and Fe elements. Fig. 2**c and d** display the Mn and Fe K-edge XANES spectra changes, respectively, during cycling. During the initial charging from the $Na_{0.67}[Mg_{0.22}Mn_{0.55}Fe_{0.23}]O_2$ phase, the Mn K-edge XANES spectra negligibly shifted until a full charging state of 4.4 V (*vs* Na^+/Na), which indicates that Mn^{4+} cations in the $Na_{0.67}[Mg_{0.22}Mn_{0.55}Fe_{0.23}]O_2$ phase wasn't further oxidized during charging to 4.4 V. On the other hand, it was observed that the pre-edge intensity is increased upon charging to 4.4 V and shifted toward higher energy for edge-crest at the same time. It was known that XANES is highly affected by the electronic and crystal structural information on the local environments neighboring target elements. The change of Mn edge-crest is the typical observation for anionic redox activity from the local Mn^{4+}–O bonding, which results from the localized holes and distortion in MnO_6 octahedra [47,48]. Thus, changes of the pre-edge after charging to 4.4 V imply the changed local environments neighboring Mn^{4+} ions by oxidized oxygen anions and the occurrence of anionic redox reaction of O^{2-}/O^- in P2-$Na_{0.67}[Mg_{0.22}Mn_{0.55}Fe_{0.23}]O_2$. However, the oxidation state of Mn shifted to 3 + after full discharging (1.5 V, to $Na_1[Mg_{0.22}Mn_{0.55}Fe_{0.23}]O_2$ phase). For the Fe K-edge XANES spectra, the oxidation state of the Fe element upon charging to 4.4 V (*vs* Na^+/Na) showed an obvious change toward higher energy level with the growth of the pre-edge peak intensity, indicating the oxidation reaction of Fe^{3+}/Fe^{4+}. The oxidation state returned to the original 3 + state after full discharge to 1.5 V.

Further oxidation of oxygen during Na^+ deintercalation can be identified in the O K-edge spectra and the differences depending on the different charge states. For investigating the bulk sensitivity on the oxidation of TM (Mn, Fe) and O during Na^+ de/intercalation, we performed the *ex-situ* O K-edge soft X-ray absorption spectroscopy (sXAS) analyses using total fluorescence yield (TFY) mode. As shown in Fig. 2**e and f**, it was verified that the intensity at ~530.4 eV in the pre-edge of O K-edge sXAS spectra is increased after charging to 4.2 V, corresponding to the preferential oxidation of the partial oxygen anions during initial Na^+ deintercalation [19,20,49–51]. Moreover, the intensity at ~530.4 eV after further charging to 4.4 V is larger than that measured at the 4.2 V-charged sample, which is attributed to oxidation of the other oxygen anions during further Na^+ deintercalation. These results indicate occurrence of gradational anionic redox reaction in P2-$Na_x[Mg_{0.22}Mn_{0.55}Fe_{0.23}]O_2$ during Na^+ de/intercalation. The gradual increase of the intensity at ~530.4 eV also implies occurrence of the gradational and sequential anionic redox reaction in $Na_x[Mg_{0.22}Mn_{0.55}Fe_{0.23}]O_2$, which is consistent with the computational results. The gradational anionic redox reaction in P2-$Na_x[Mg_{0.22}Mn_{0.55}Fe_{0.23}]O_2$ was also confirmed through *ex-situ* XPS analyses. **Fig. S5** shows that the peak intensity at ~530.5 eV related to the peroxo-like (O^-) species in O 1*s* XPS spectra was observed after initially charging to 4.2 V, and then the peak intensity was more increased after further charging to 4.4 V by gradationally occurred O^{2-}/O^- redox reaction. After discharging to 1.5 V, the peak of the peroxo-like species was disappeared [52–54]. In addition, the anionic redox reaction of oxygen anion in various previous studies was expressed to O^{2-}/O^- or $O^{2-}/(O_2)^{n-}$ (n ≥ 2). [28,29,45,55,56] When the oxygen anions (O^{2-}) are oxidized during charge, the O^- species are produced. Owing to instability of O^-, moreover, two O^- species can be transformed to O^{2-} and O^0 ($2O^- \rightarrow O^{2-} + O^0$). Since O^{2-} ions attempt to be stabilized by covalent bonds, they form peroxo-like O—O dimers, $(O_2)^{n-}$ ($n \geq 2$) [57,58]. Thus, it was known that peroxo-like dimer species can be formed at the transition metal layers of the layered oxide cathodes for SIB and LIB, as oxidation of O^{2-} can provide the driving force for oxygen dimerization [59]. Although the final product after oxidation of oxygen anion is $(O_2)^{n-}$, we used expression of the anionic redox reaction as O^{2-}/O^- to focus the direct oxidation and reduction of oxygen anions occurred during charge/discharge.

3.3. Gradational and selective redox reaction of oxygen anions in P2-$Na_x[Mg_{0.22}Mn_{0.55}Fe_{0.23}]O_2$

The predicted projected density of states (pDOS) of Mn, Fe, and O was calculated through density functional theory (DFT) calculations to further investigate the details of the oxygen-redox process in $Na_x[Mg_{0.22}Mn_{0.55}Fe_{0.23}]O_2$ ($0 \leq x \leq 1$). Fig. 3**a** shows the pDOS of $Na_1[Mg_{0.22}Mn_{0.55}Fe_{0.23}]O_2$ (fully discharged state). In this state, the electron density of Mn 3*d* orbitals is closest to the Fermi level (E_F). During Na^+ deintercalation from $Na_{0.75}[Mg_{0.22}Mn_{0.55}Fe_{0.23}]O_2$, the occupied Mn 3*d* density is reduced and the hole density above the Fermi level is increased, confirming the Mn^{3+}/Mn^{4+} redox reaction (Fig. 3**b**). Then, the electron densities occupied in the Fe 3*d* and O 2*p* states were simultaneously active near the Fermi level, and the hole densities in pDOS of Fe and O were created when going from $Na_{0.75}[Mg_{0.22}Mn_{0.55}Fe_{0.23}]O_2$ (Fig. 3**b**) to $Na_{0.5}[Mg_{0.22}Mn_{0.55}Fe_{0.23}]O_2$ (Fig. 3**c**), indicating the presence of anionic-redox-preferred Fe 3*d*–O 2*p*

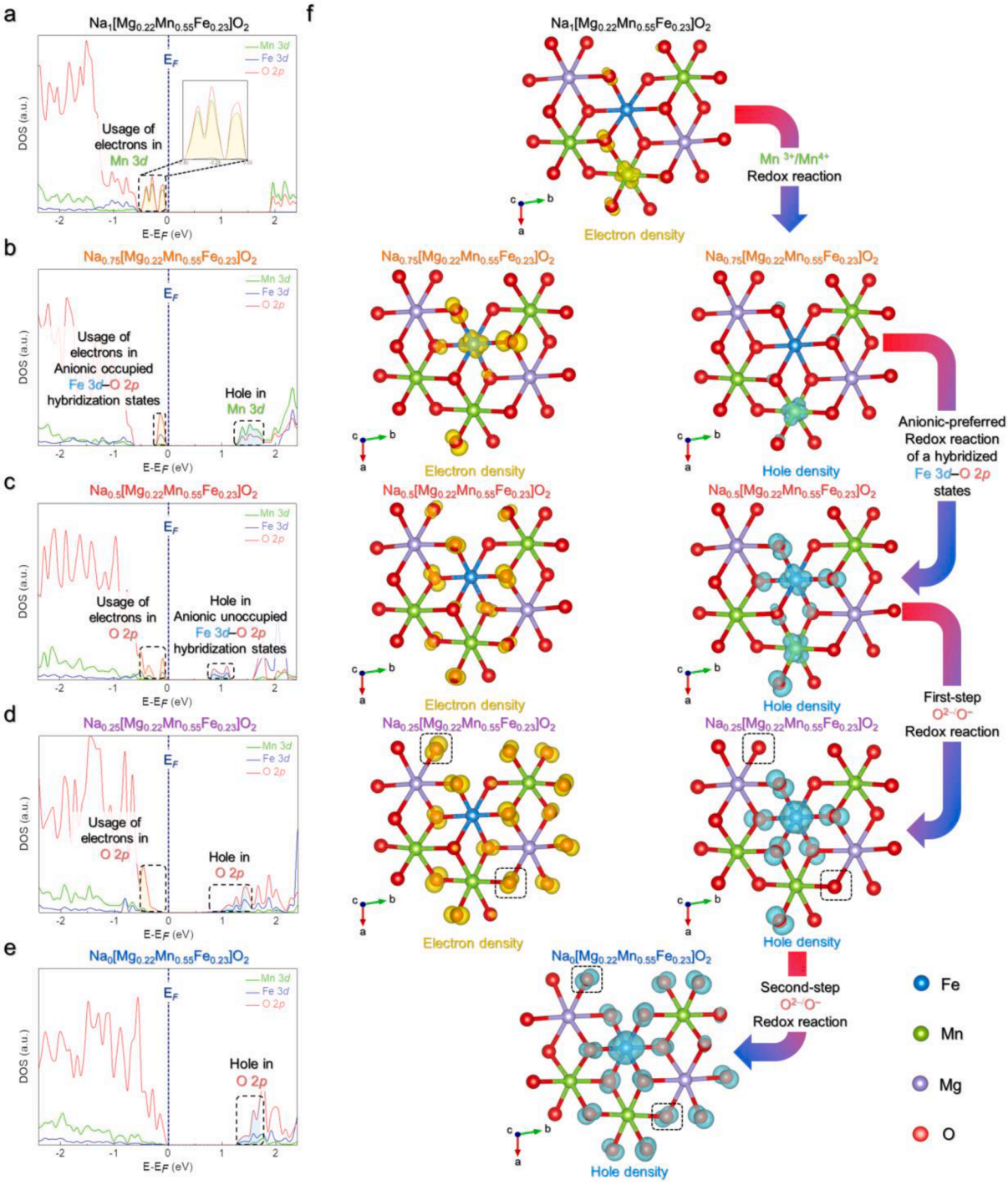

Fig. 3. pDOS TM (Mn, Fe) 3*d* and O 2*p* orbitals of (a) $Na_1[Mg_{0.22}Mn_{0.55}Fe_{0.23}]O_2$, (b) $Na_{0.75}[Mg_{0.22}Mn_{0.55}Fe_{0.23}]O_2$, (c) $Na_{0.5}[Mg_{0.22}Mn_{0.55}Fe_{0.23}]O_2$, (d) $Na_{0.25}[Mg_{0.22}Mn_{0.55}Fe_{0.23}]O_2$, and (e) $Na_0[Mg_{0.22}Mn_{0.55}Fe_{0.23}]O_2$. (f) Visualized pDOS TM (Mn, Fe) 3*d* and O 2*p* orbitals between $Na_0[Mg_{0.22}Mn_{0.55}Fe_{0.23}]O_2$ and $Na_1[Mg_{0.22}Mn_{0.55}Fe_{0.23}]O_2$: electron density (yellow) and hole density (blue). (For interpretation of the references to colour in this figure legend, the reader is referred to the web version of this article.)

hybridized orbital states. Upon further charging to $Na_{0.25}[Mg_{0.22}Mn_{0.55}Fe_{0.23}]O_2$ (Fig. 3**d**), the electron density change of the O 2*p* orbitals was dominant, and hole density in O 2*p* above the Fermi level was created. After further extraction to $Na_0[Mg_{0.22}Mn_{0.55}Fe_{0.23}]O_2$ (Fig. 3**e**), the hole density gradually increased in the O 2*p* orbitals, resulting from gradational occurrence of oxygen oxidation. Changes of the pDOS and the visualization of charge densities in $Na_x[Mg_{0.22}Mn_{0.55}Fe_{0.23}]O_2$ with different Na contents were well matched with variation in integrated spin moments of Mn, Fe, and O depending on the Na contents in the structure.

The visualized electron and hole densities indicated a series of gradational and sequential oxidation of oxygen anions in $Na_x[Mg_{0.22}Mn_{0.55}Fe_{0.23}]O_2$ during desodiation ($0 \leq x \leq 1$) (Fig. 3**f**). During Na^+ deintercalation from $Na_1[Mg_{0.22}Mn_{0.55}Fe_{0.23}]O_2$ to $Na_{0.75}[Mg_{0.22}Mn_{0.55}Fe_{0.23}]O_2$, it was confirmed that the Mn^{3+}/Mn^{4+} redox reaction was mainly performed through a change from electron densities to hole densities of Mn 3*d* orbitals. In the case of $Na_{0.75}[Mg_{0.22}Mn_{0.55}Fe_{0.23}]O_2$, electron densities co-existed in Fe 3*d* and

O 2*p* orbitals below the Fermi level. It was observed that the electron densities of both Fe 3*d* and O 2*p* orbitals were transformed to hole densities between $Na_{0.75}[Mg_{0.22}Mn_{0.55}Fe_{0.23}]O_2$ and $Na_{0.5}[Mg_{0.22}Mn_{0.55}Fe_{0.23}]O_2$, indicating the use of electrons in anionic-redox-preferred Fe 3*d*–O 2*p* hybridized orbital states. It was also implied that the Fe cations and O anions simultaneously contribute to the capacity in $Na_x[Mg_{0.22}Mn_{0.55}Fe_{0.23}]O_2$ through the anionic-redox-preferred reaction of hybridized Fe 3*d*–O 2*p* orbital states. Notably, as the first step, the electron densities of O 2*p* orbitals neighboring Fe and Mn cations mainly participate in the anionic redox reaction, for deintercalation of 0.25 mol Na^+ from $Na_{0.5}[Mg_{0.22}Mn_{0.55}Fe_{0.23}]O_2$ to $Na_{0.25}[Mg_{0.22}Mn_{0.55}Fe_{0.23}]O_2$. And then, O 2*p* orbitals neighboring Mg cations provide the additional anionic redox reaction from $Na_{0.25}[Mg_{0.22}Mn_{0.55}Fe_{0.23}]O_2$ to $Na_0[Mg_{0.22}Mn_{0.55}Fe_{0.23}]O_2$ as the second step. The oxygen anions adjacent to the Mg cations in dotted circles provide holes for localized desodiation forming the various local coordination environments. In terms of the general anion redox reaction of O^{2-}/O^-, it was reported that all oxygen anions in the structure simultaneously undergo the anionic redox reaction, and the oxidized oxygen anions exhibit the strong reactivity for attracting electrons from other ions [19,57,60,61]. The oxidized oxygen anions are going to be close to each other for sharing their electrons. Thus, the large structural distortion by high reactivity of oxidized oxygen anions can be occurred during anionic redox reaction, which is regarded as one of the reasons on in poor electrochemical performances of anionic-redox-based cathode materials [19,20]. However, DFT calculation results indicate that partial oxygen anions in P2-$Na_x[Mg_{0.22}Mn_{0.55}Fe_{0.23}]O_2$ are preferentially oxidized during Na^+ deintercalation and the oxidized and non-oxidized oxygen anions co-exist even at the charged state. After full oxidation of initially oxidized oxygen anionic, the other oxygen anions are gradationally participated in the redox reaction. These phenomena are different from the general anionic redox reaction based on simultaneous oxidation of all oxygen anions. These results also imply that the direct contact of oxidized oxygen anions and the corresponding large structural distortion can be suppressed in P2-$Na_x[Mg_{0.22}Mn_{0.55}Fe_{0.23}]O_2$ structure by existence of non-oxidized oxygen anions in the charged state. Thus, we expected that P2-$Na_x[Mg_{0.22}Mn_{0.55}Fe_{0.23}]O_2$ can deliver the outstanding electrochemical performances by gradational anionic redox reaction.

Further theoretical and experimental works reveal that the local structural environment in $Na_x[Mg_{0.22}Mn_{0.55}Fe_{0.23}]O_2$, such as the change of $[TM]O_6$ octahedra, is stably retained without severe changes even after anionic redox reaction. Through DFT calculation, we compared the Mn–O and Fe–O bonding distance between $Na_0[Mg_{0.22}Mn_{0.55}Fe_{0.23}]O_2$ and $Na_{0.5}[Mg_{0.22}Mn_{0.55}Fe_{0.23}]O_2$. As tabulated in Fig. 4**a**, the average local bonding distance of Mn–O and Fe–O decreased from ≈2.02 to ≈ 1.94 Å and from ≈2.00 to ≈1.91 Å, respectively, during Na^+ deintercalation by the oxidation of oxygen anions. Furthermore, Fig. 4**b and c** show the Mn–O and Fe–O bonding distances, respectively, in $Na_x[Mg_{0.22}Mn_{0.55}Fe_{0.23}]O_2$ ($0 \leq x \leq 1$)

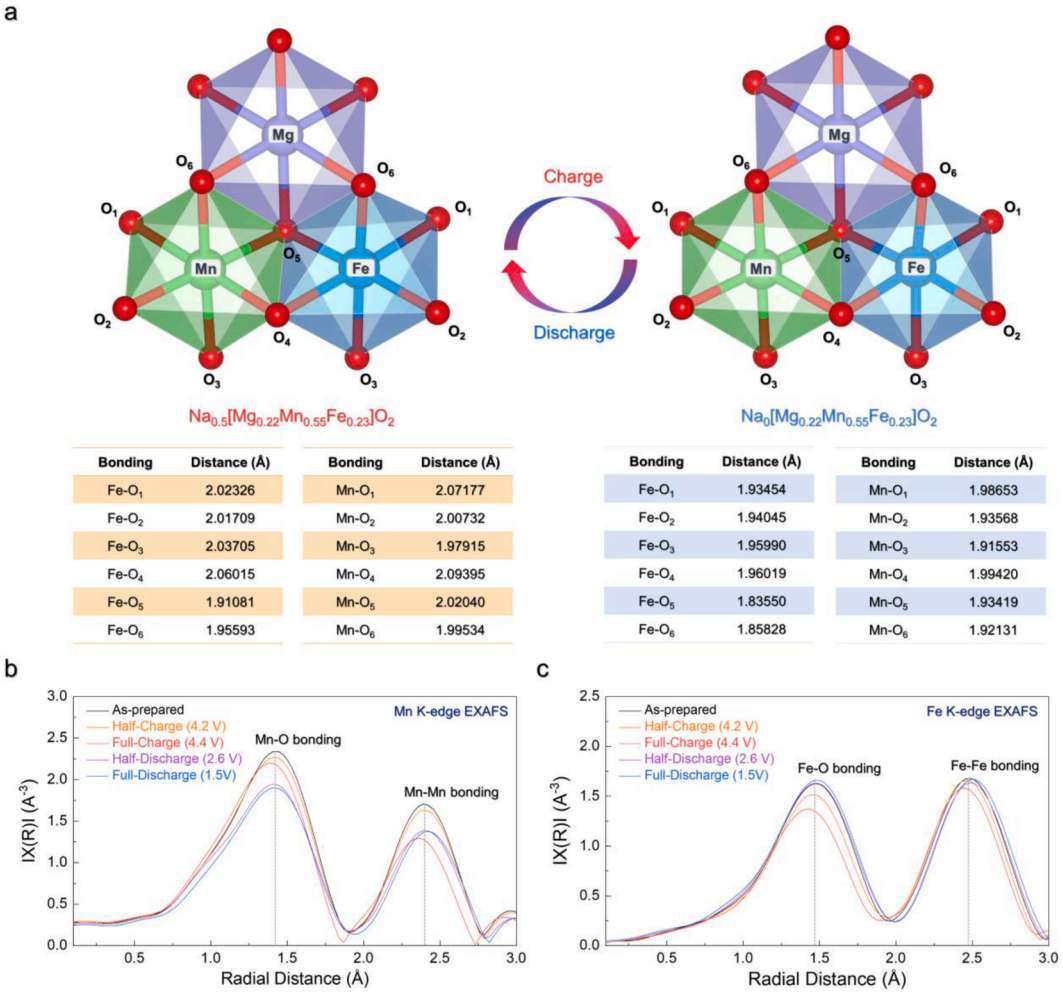

Bonding	Distance (Å)	Bonding	Distance (Å)
Fe-O_1	2.02326	Mn-O_1	2.07177
Fe-O_2	2.01709	Mn-O_2	2.00732
Fe-O_3	2.03705	Mn-O_3	1.97915
Fe-O_4	2.06015	Mn-O_4	2.09395
Fe-O_5	1.91081	Mn-O_5	2.02040
Fe-O_6	1.95593	Mn-O_6	1.99534

Bonding	Distance (Å)	Bonding	Distance (Å)
Fe-O_1	1.93454	Mn-O_1	1.98653
Fe-O_2	1.94045	Mn-O_2	1.93568
Fe-O_3	1.95990	Mn-O_3	1.91553
Fe-O_4	1.96019	Mn-O_4	1.99420
Fe-O_5	1.83550	Mn-O_5	1.93419
Fe-O_6	1.85828	Mn-O_6	1.92131

Fig. 4. (a) Comparison of predicted Fe–O and Mn–O bonding distances of [Mg, Mn, Fe]O_6 octahedra $Na_0[Mg_{0.22}Mn_{0.55}Fe_{0.23}]O_2$ and $Na_{0.5}[Mg_{0.22}Mn_{0.55}Fe_{0.23}]O_2$. *Ex-situ* EXAFS analyses of various charge/discharge state of $Na_{0.67}[Mg_{0.22}Mn_{0.55}Fe_{0.23}]O_2$ with (b) Mn–O and Mn–Mn bonding distances and (c) Fe–O and Fe–Fe bonding distances.

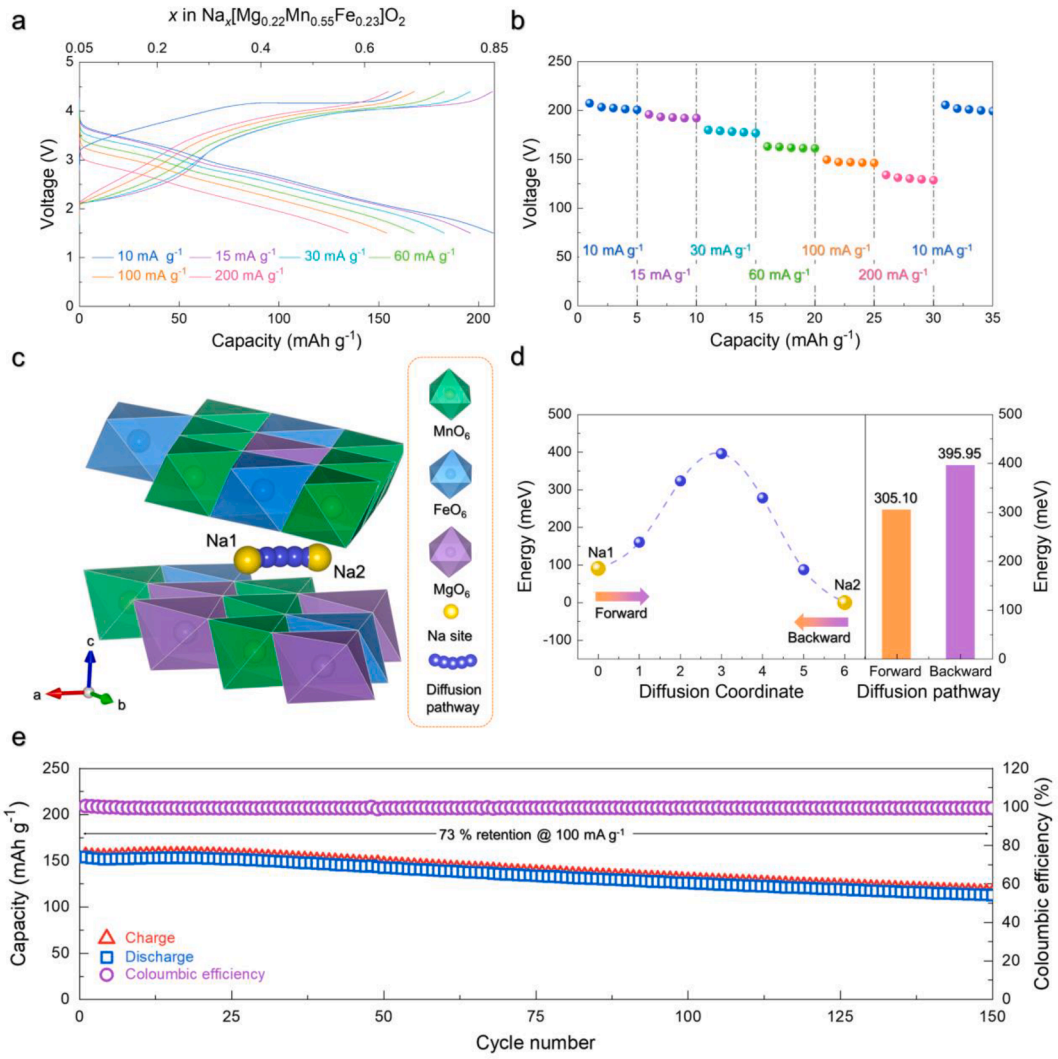

Fig. 5. (a) Charge/Discharge profiles of Na$_x$[Mg$_{0.22}$Mn$_{0.55}$Fe$_{0.23}$]O$_2$ in the voltage range of 1.5–4.4 V at various current densities. (b) Power capability of Na$_{0.67}$[Mg$_{0.22}$Mn$_{0.55}$Fe$_{0.23}$]O$_2$ at various current densities. (c) Predicted diffusion pathway for Na$^+$ and (d) activation barrier energy for Na$^+$ diffusion using the NEB method in Na$_{0.67}$[Mg$_{0.22}$Mn$_{0.55}$Fe$_{0.23}$]O$_2$. (e) Cycle performance of Na$_{0.67}$[Mg$_{0.22}$Mn$_{0.55}$Fe$_{0.23}$]O$_2$ in the voltage of 1.5–4.4 V during 150 cycles at 100 mA g^{-1}.

obtained by Fourier-transform *ex-situ* extended X-ray absorption fine structure (FT-EXAFS) analyses. The bonding distances of Mn–O or Fe–O during charge/discharge monotonously changed. Moreover, the peak shape of FT-EXAFS was well retained during charge/discharge, which implies that there is no severe distortion on local environment of the TM–O octahedral in Na$_x$[Mg$_{0.22}$Mn$_{0.55}$Fe$_{0.23}$]O$_2$ during the redox reactions. To verify the change of local environments in Na$_x$[Mg$_{0.22}$Mn$_{0.55}$Fe$_{0.23}$]O$_2$ during charge/discharge more accurately, we further performed the fitting on the *ex-situ* FT-EXAFS data of Na$_x$[Mg$_{0.22}$Mn$_{0.55}$Fe$_{0.23}$]O$_2$. Here, we used the radial distribution functions of k^3-weight conditions in the fitting range of 1.0–2.0 Å for the first shell, corresponding to the TM–O bonds. The amplitude reduction factor (S_0^2) is 1.0. As shown in **Fig. S6 and S7**, it was verified that the total maximum changes of average bonding distances on Mn–O and Fe–O during charge/discharge are just ~1.80 %, which indicates the small structural change of Na$_x$[Mg$_{0.22}$Mn$_{0.55}$Fe$_{0.23}$]O$_2$ during the redox reactions. These EXAFS results are well matched with the first-principles calculations results showing the change of TM–O bonding distances during Na$^+$ de/intercalation.

3.4. *Outstanding electrochemical performance of P2-Na$_{0.67}$[Mg$_{0.22}$Mn$_{0.55}$Fe$_{0.23}$]O$_2$ stemming from high structural stability*

Fig. 5**a and b** present the charge/discharge profiles and discharge capacities of Na$_{0.67}$[Mg$_{0.22}$Mn$_{0.55}$Fe$_{0.23}$]O$_2$, respectively, measured at various current densities in the voltage range of 1.5–4.4 V (*vs* Na$^+$/Na). Even at 200 mA g^{-1}, the specific capacity of Na$_{0.67}$[Mg$_{0.22}$Mn$_{0.55}$Fe$_{0.23}$]O$_2$ was ~134.6 mAh g^{-1}, which is ~65 % of that measured at 10 mA g^{-1} with the average redox potential of ~2.81 V (*vs* Na$^+$/Na). The practical capacity was well recovered when returning to a low current density of 10 mA g^{-1}. This outstanding power capability is associated with a low activation barrier of Na hopping. The theoretical calculation of the activation barrier energy for Na$^+$ diffusion pathways using the nudged elastic band (NEB) method is shown in Fig. 5**c**. For Na$_{0.67}$[Mg$_{0.22}$Mn$_{0.55}$Fe$_{0.23}$]O$_2$, Na$^+$ ions located in the prismatic site diffuse to the adjacent prismatic site to retain a stable structure (Fig. 5**c**). The predicted activation energy required along Na1–Na2 was calculated to be 395.95 meV, as shown in Fig. 5**d**, which is considered sufficiently low energy for facile Na$^+$ diffusion in the Na$_{0.67}$[Mg$_{0.22}$Mn$_{0.55}$Fe$_{0.23}$]O$_2$ structure. Na$_{0.67}$[Mg$_{0.22}$Mn$_{0.55}$Fe$_{0.23}$]O$_2$ retained ~73 % of the initial capacity after 150 cycles at the identical charge/discharge current density of 100 mA g^{-1}, with a high coulombic efficiency of > ~99 % (Fig. 5**e**), indicating the excellent cycle life. Moreover, we performed

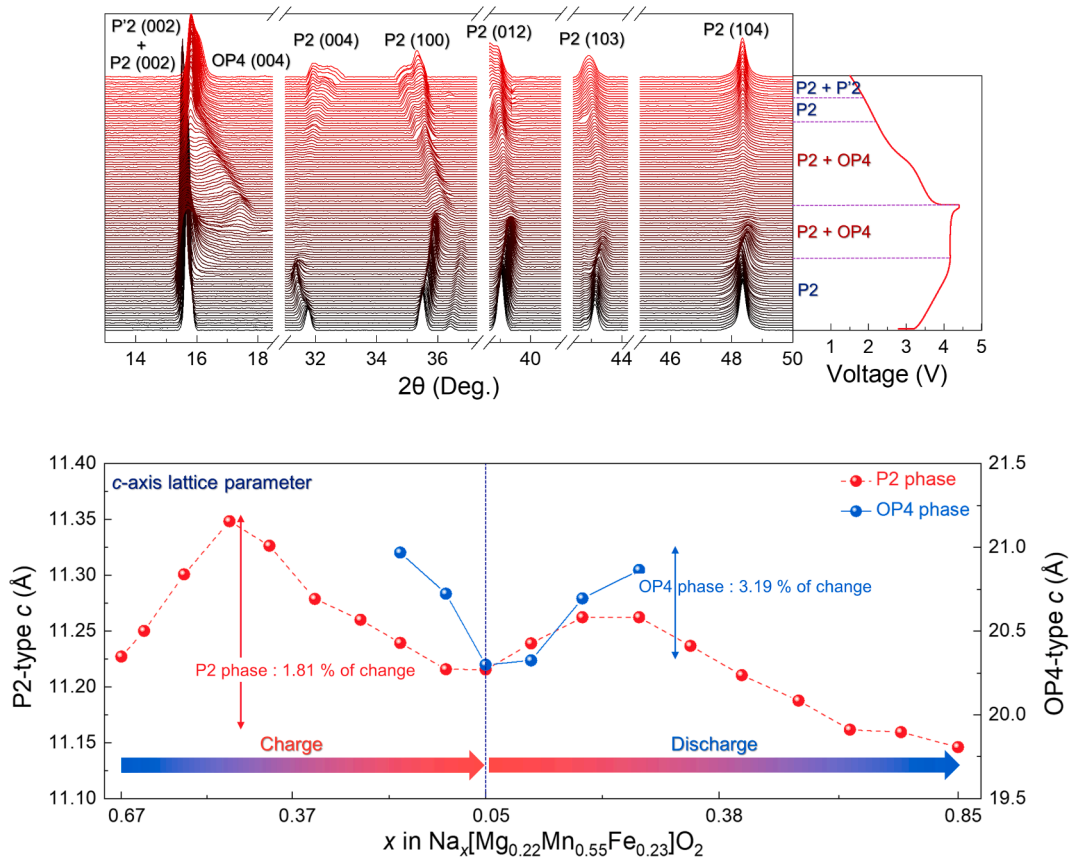

Fig. 6. (a) *Ex-situ* magnified view of *operando* XRD pattern of $Na_{0.67}[Mg_{0.22}Mn_{0.55}Fe_{0.23}]O_2$ during charge/discharge. (b) Change in *c*-axis lattice parameters of $Na_x[Mg_{0.22}Mn_{0.55}Fe_{0.23}]O_2$ in the structure during charge/discharge.

full-cell tests of P2-$Na_{0.67}[Mg_{0.22}Mn_{0.55}Fe_{0.23}]O_2$ using hard carbon anode with the N/P capacity ratio of 1.2. **Fig. S8a** shows that the $Na_{0.67}[Mg_{0.22}Mn_{0.55}Fe_{0.23}]O_2$‖hard carbon full-cell delivered a specific capacity of ~203 mAh g^{-1} at 10 mA g^{-1} in the range of 1.4–4.3 V (*vs* Na^+/Na). Especially, it was verified that the capacity retention of the full-cell for 150 cycles at 100 mA g^{-1} was ~71.8 % with a high coulombic efficiency of above ~99 % (**Fig. S8b**), which indicates the outstanding cycle performance of $Na_{0.67}[Mg_{0.22}Mn_{0.55}Fe_{0.23}]O_2$ under the full cell system.

To demonstrate the effect on the substitution degree of Mg^{2+} cations, we prepared P2-$Na_{0.67}[Mg_xMn_{0.55}Fe_{0.45-x}]O_2$ ($x = 0.11$) with different Mg^{2+} contents. As shown in **Fig. S9** and **Table S3** below, it was verified that the $Na_{0.67}[Mg_xMn_{0.55}Fe_{0.45-x}]O_2$ ($x = 0.11$) samples exhibited the P2-type layered structure without impurities. In addition, we compare the cycle-performances of P2-$Na_{0.67}[Mg_{0.22}Mn_{0.55}Fe_{0.23}]O_2$ and P2-$Na_{0.67}[Mg_{0.11}Mn_{0.55}Fe_{0.34}]O_2$. As shown in **Fig. S10** below, it was verified that P2-$Na_{0.67}[Mg_{0.22}Mn_{0.55}Fe_{0.23}]O_2$ delivered better cycle performance at the same conditions than P2-$Na_{0.67}[Mg_{0.11}Mn_{0.55}Fe_{0.34}]O_2$. These results indicate that the Mg contents of 0.22 mol is required for stable anionic redox reaction in P2-type Na-Fe-Mn-O cathode materials. Most sodium layered oxide cathodes suffer from poor cycle retention, which stems from the severe oxygen framework change due to the Na de/sodiation chemistry [62]. Nonetheless, P2-$Na_{0.67}[Mg_{0.22}Mn_{0.55}Fe_{0.23}]O_2$ exhibits remarkable cycle retention. To monitor the structural evolution during Na^+ de/intercalation, we performed *operando* XRD (*o*-XRD) analyses in the voltage range of 1.5–4.4 V (*vs* Na^+/Na) (Fig. 6**a**). As shown in Fig. 6**a**, the XRD peaks corresponding to the (002) plane of the P2 phase monotonically shifted toward lower 2θ angles during the initial charging. This is due to the enlarged electrostatic repulsion between adjacent transition-metal layers, resulting in expansion of the *c*-axis lattice parameter [63]. The (002) peak was split into (002) and (004) peaks for P2 and OP4 phases, respectively, upon further charging. When the voltage increased to close to 4.4 V, the intensity of the (002) peak belonging to the P2 phase decreased slightly. The intensity of the (004) peak of the OP4 phase gradually increased; however, the electrode still majorly consisted of the P2 phase according to the XRD pattern. This observation is identical to a relaxed phase transition, as shown in the *ex-situ* XRD analyses of $Na_{0.67}[Mg_{0.22}Mn_{0.55}Fe_{0.23}]O_2$ (**Fig. S11**). During discharging to 2.6 V, the (004) peak of the OP4 phase gradually shifted to low 2θ angle and eventually merged with the P2 phase (Fig. 6**a**). At the end of discharge to 1.5 V, the (002) peak shifted to higher 2θ angle with formation of the P'2 phase [64]. The P2-OP4 phase transition in P2-$Na_{0.67}[Mg_{0.22}Mn_{0.55}Fe_{0.23}]O_2$ is also well matched with the previous researches showing that the Mg-substitution in P2-type Mn-based cathode materials can lead to the P2(ABBA)-OP4(ABBACAAC) phase transition during charge/discharge with suppression of P2(ABBA)–O2 (ABAC) phase transition [42,65,66]. This *ex-situ* XRD result is the reason why we used the formation energies between P2 and OP4 in the structure of P2-$Na_{0.67}[Mg_{0.22}Mn_{0.55}Fe_{0.23}]O_2$ through DFT calculation.

The oxygen stacking transition from the P2 to OP4 phase occurs by slab gliding between transition-metal oxide layers in the high-voltage (4.1–4.3 V) range [66,67]. The structure of the intermediate OP4 phase consists of a stack of mixed octahedral and prismatic structures along the *c*-axis direction [68]. According to previous reports [17,69], the OP4 phase appears solely at a charged state, and this is the major reason for the structural degradation of P2-type layered-oxide cathodes. However, in case of P2-$Na_{0.67}[Mg_{0.22}Mn_{0.55}Fe_{0.23}]O_2$, the OP4 phase comes out partially even at a fully charged state, not showing full phase transition as shown in Fig. 6**a** after charging to 4.4 V. Thus, we supposed that the phase transition to the OP4 phase is relatively suppressed in P2-$Na_{0.67}[Mg_{0.22}Mn_{0.55}Fe_{0.23}]O_2$. To compare the effect of the redox

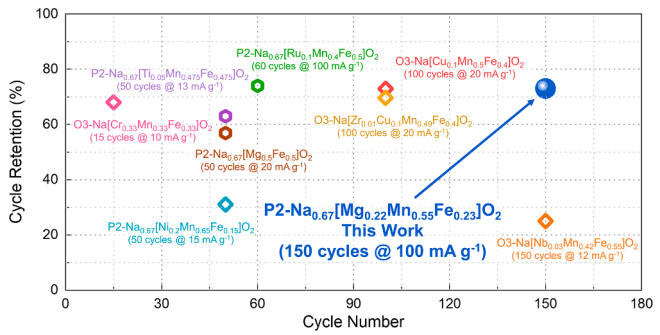

Fig. 7. Comparison of the cycle performance of $Na_{0.67}[Mg_{0.22}Mn_{0.55}Fe_{0.23}]O_2$ and other Mn-Fe-based layered cathodes for NIBs.

inactive element on suppression of P2-OP4 phase transition, we measured the *ex-situ* XRD patterns of P2-$Na_{0.67}[Mg_{0.11}Mn_{0.55}Fe_{0.34}]O_2$ with small amount of Mg^{2+} cation. As shown in **Fig. S12**, it was verified that the P2 phase was clearly disappeared after full charging process of P2-$Na_{0.67}[Mg_{0.11}Mn_{0.55}Fe_{0.34}]O_2$ and the OP4 phase was only observed. In addition, the maximum *c* lattice variation in each P2 and OP4 phase was ~1.81 % and ~3.19 %, respectively, imposing a low-level internal strain on the structure (Fig. 6**b**). Moreover, we investigated the changes in the morphology and crystal structure of P2-$Na_{0.67}[Mg_{0.22}Mn_{0.55}Fe_{0.23}]O_2$ after prolonged cycling using *ex-situ* SEM and XRD analyses. All samples are prepared at 100 mA g^{-1} during charge/discharge. As shown in **Fig. S13 and S14**, it was verified that the morphology and structure of P2-$Na_{0.67}[Mg_{0.22}Mn_{0.55}Fe_{0.23}]O_2$ particles were well retained without severe degradation after 150 cycles, which is connected with the outstanding cyclability of P2-$Na_{0.67}[Mg_{0.22}Mn_{0.55}Fe_{0.23}]O_2$.

Furthermore, we compared the electrochemical performances among P2-$Na_{0.67}[Mg_{0.22}Mn_{0.55}Fe_{0.23}]O_2$ and other TM-doped P2-$Na_y[Mn_xFe_{1-x}]O_2$[16,22–27] (Fig. 7), which indicates that P2-$Na_{0.67}[Mg_{0.22}Mn_{0.55}Fe_{0.23}]O_2$ delivered the outstanding cycle performance as the anionic-redox-based cathode for NIBs. (The detailed comparison information of Mn and Fe-based layered oxide cathodes for Na-ion batteries is summarized in **Table S4**, Supporting Material). Like the existing Mn and Fe cations, the doped TM cations also experience the redox reaction during charge/discharge. By the redox reactions of not only the existing Mn and Fe cations but also the doped TM cations, the bonding interaction between TM cation (doped TM, Mn, and Fe) and O anion in TM-doped P2-$Na_y[Mn_xFe_{1-x}]O_2$ is largely changed during Na^+ de/intercalation, which implies TM-doping cannot efficiently suppress the structural changes in P2-$Na_y[Mn_xFe_{1-x}]O_2$ occurred during Na^+ de/intercalation. On the other hand, P2-$Na_{0.67}[Mg_{0.22}Mn_{0.55}Fe_{0.23}]O_2$ structure can be stably retained during charge/discharge since Mg^{2+} cation with fixed oxidation state cannot be oxidized/reduced during charge/discharge, which is confirmed through the fitting on the *ex-situ* FT-EXAFS data (**Fig. S6 and S7**). Thus, substitution of Mg^{2+} cations can effectively lead to the small change of local structural environments in anionic-redox-based P2-$Na_y[Mn_xFe_{1-x}]O_2$ during Na^+ de/intercalation, which leads to the outstanding electrochemical performances of P2-$Na_{0.67}[Mg_{0.22}Mn_{0.55}Fe_{0.23}]O_2$. These results suggest that P2-$Na_{0.67}[Mg_{0.22}Mn_{0.55}Fe_{0.23}]O_2$, which undergoes small structural and morphological variation during Na^+ de/intercalation by both cationic and anionic redox reactions, exhibits outstanding cycling performance as a promising cathode for NIBs.

4. Conclusion

In this work, we demonstrated that P2-$Na_{0.67}[Mg_{0.22}Mn_{0.55}Fe_{0.23}]O_2$ can deliver outstanding electrochemical performance *via* high structural stability while the anionic redox reaction of O^{2-}/O^- occurs during Na^+ de/intercalation. At 10 mA g^{-1} in the voltage range of 1.5–4.4 V (*vs* Na^+/Na), P2-$Na_{0.67}[Mg_{0.22}Mn_{0.55}Fe_{0.23}]O_2$ delivered a large specific capacity of ~207 mAh g^{-1}, corresponding to ~0.8 mol Na^+ de/intercalation. Most importantly, up to ~73 % of the initial capacity was retained with a high coulombic efficiency of > 99 % for 150 cycles at 100 mA g^{-1}, indicating the excellent cycle performance with the stable O^{2-}/O^- redox reaction. Through combined studies using DFT calculation and various experimental techniques, it was verified that the stable electrochemical behaviors of anionic-redox-based P2-$Na_{0.67}[Mg_{0.22}Mn_{0.55}Fe_{0.23}]O_2$ are attributed to the small change of the local environments by gradational and selective anionic redox reactions, which is consistent with the well-retained structure and morphology without severe degradation after prolonged cycling. Furthermore, from a cost perspective, the composition based on earth-abundant elements without expensive elements such as Ni, Co, *etc.* is one of the most attractive merits of the P2-$Na_{0.67}[Mg_{0.22}Mn_{0.55}Fe_{0.23}]O_2$ cathode with large practical capacity, enabling low-cost and high-energy Na-ion batteries. We believe that this research will provide meaningful insight into understanding the stabilization of the anionic redox reaction in layered oxide cathode materials for not only Na-ion batteries but also other rechargeable batteries.

Data availability

Data will be made available on request.

Declaration of Competing Interest

The authors declare that they have no known competing financial interests or personal relationships that could have appeared to influence the work reported in this paper.

Acknowledgements

This research was supported by the National Research Foundation of Korea funded by the Ministry of Science and ICT of Korea (NRF-2021R1A2C1014280, NRF-2020M2D8A2070870, NRF-2022M3H4A1A01010832, and 2019M3D1A2104105) and The calculation resources were supported by the Supercomputing Center in Korea Institute of Science and Technology Information (KSC-2021-CRE-0447).

Appendix A. Supplementary data

Supplementary data to this article can be found online at https://doi.org/10.1016/j.cej.2022.138883.

References

[1] D. Larcher, J.M. Tarascon, Towards greener and more sustainable batteries for electrical energy storage, Nat. Chem. 7 (2015) 19–29, https://doi.org/10.1038/nchem.2085.
[2] J.P. Holdren, Energy and Sustainability, Science 315 (5813) (2007).
[3] K. Caldeira, J.F. Kasting, Insensitivity of global warming potentials to carbon dioxide emission scenarios, Nature. 366 (1993) 251–253, https://doi.org/10.1038/366251a0.
[4] M. Armand, J.-M. Tarascon, Building better batteries, Nature. 451 (2008) 652–657, https://doi.org/10.1038/451652a.
[5] W. Choi, H.C. Shin, J.M. Kim, J.Y. Choi, W.S. Yoon, Modeling and Applications of Electrochemical Impedance Spectroscopy (EIS) for Lithium-ion Batteries, J. Electrochem. Sci. Technol. 11 (2020) 1–13, https://doi.org/10.33961/jecst.2019.00528.
[6] T. Kim, W. Choi, H.C. Shin, J.Y. Choi, J.M. Kim, M.S. Park, W.S. Yoon, Applications of Voltammetry in Lithium Ion Battery Research, J. Electrochem. Sci. Technol. 11 (2020) 14–25, https://doi.org/10.33961/jecst.2019.00619.
[7] Y. Miao, P. Hynan, A. Von Jouanne, A. Yokochi, Current Li-Ion Battery Technologies in Electric Vehicles and Opportunities for Advancements, Energies. 12 (2019) 1–20, https://doi.org/10.3390/en12061074.
[8] S.W. Kim, D.H. Seo, X. Ma, G. Ceder, K. Kang, Electrode Materials for Rechargeable Sodium-Ion Batteries: Potential Alternatives to Current Lithium-Ion Batteries, Adv. Energy Mater. 2 (2012) 710–721, https://doi.org/10.1002/aenm.201200026.
[9] H. Pan, Y.S. Hu, L. Chen, Room-temperature stationary sodium-ion batteries for large-scale electric energy storage, Energy Environ. Sci. 6 (2013) 2338–2360, https://doi.org/10.1039/c3ee40847g.

[10] K. Kubota, N. Yabuuchi, H. Yoshida, M. Dahbi, S. Komaba, Layered oxides as positive electrode materials for Na-ion batteries, MRS Bull. 39 (2014) 416–422, https://doi.org/10.1557/mrs.2014.85.

[11] T. Jin, H. Li, K. Zhu, P.F. Wang, P. Liu, L. Jiao, Polyanion-type cathode materials for sodium-ion batteries, Chem. Soc. Rev. 49 (2020) 2342–2377, https://doi.org/10.1039/c9cs00846b.

[12] Z. Gong, Y. Yang, Recent advances in the research of polyanion-type cathode materials for Li-ion batteries, Energy Environ. Sci. 4 (2011) 3223–3242, https://doi.org/10.1039/c0ee00713g.

[13] Y. Lu, L. Wang, J. Cheng, J.B. Goodenough, Prussian blue: A new framework of electrode materials for sodium batteries, Chem. Commun. 48 (2012) 6544–6546, https://doi.org/10.1039/c2cc31777j.

[14] B. Wang, Y. Han, X. Wang, N. Bahlawane, H. Pan, M. Yan, Y. Jiang, Prussian Blue Analogs for Rechargeable Batteries, IScience. 3 (2018) 110–133, https://doi.org/10.1016/j.isci.2018.04.008.

[15] B. Mortemard de Boisse, D. Carlier, M. Guignard, L. Bourgeois, C. Delmas, P2-$Na_xMn_{1/2}Fe_{1/2}O_2$ Phase Used as Positive Electrode in Na Batteries: Structural Changes Induced by the Electrochemical (De)intercalation Process, Inorg. Chem. 53 (2014) 11197–11205, https://doi.org/10.1021/ic5017802.

[16] K. Tang, Y. Wang, X. Zhang, S. Jamil, Y. Huang, S. Cao, X. Xie, Y. Bai, X. Wang, Z. Luo, G. Chen, High-performance P2-Type Fe/Mn-based oxide cathode materials for sodium-ion batteries, Electrochim. Acta. 312 (2019) 45–53, https://doi.org/10.1016/j.electacta.2019.04.183.

[17] S. Kumakura, Y. Tahara, K. Kubota, K. Chihara, S. Komaba, Sodium and Manganese Stoichiometry of P2-Type $Na_{2/3}MnO_2$, Angew. Chemie - Int. Ed. 55 (2016) 12760–12763, https://doi.org/10.1002/anie.201606415.

[18] J. Billaud, G. Singh, A.R. Armstrong, E. Gonzalo, V. Roddatis, M. Armand, T. Rojo, P.G. Bruce, $Na_{0.67}Mn_{1-x}Mg_xO_2$ ($0 \leq x \leq 0.2$): a high capacity cathode for sodium-ion batteries, Energy Environ. Sci. 7 (2014) 1387–1391, https://doi.org/10.1039/c4ee00465e.

[19] J. Hong, W.E. Gent, P. Xiao, K. Lim, D.-H. Seo, J. Wu, P.M. Csernica, C.J. Takacs, D. Nordlund, C.-J. Sun, K.H. Stone, D. Passarello, W. Yang, D. Prendergast, G. Ceder, M.F. Toney, W.C. Chueh, Metal–oxygen decoordination stabilizes anion redox in Li-rich oxides, Nat. Mater. 18 (2019) 256–265, https://doi.org/10.1038/s41563-018-0276-1.

[20] W.E. Gent, I.I. Abate, W. Yang, L.F. Nazar, W.C. Chueh, Design Rules for High-Valent Redox in Intercalation Electrodes, Joule. 4 (2020) 1369–1397, https://doi.org/10.1016/j.joule.2020.05.004.

[21] P. Hou, F. Li, H. Zhang, H. Huang, Stabilizing the cationic/anionic redox chemistry of Li-rich layered cathodes by tuning the upper cut-off voltage for high energy-density lithium-ion batteries, J. Mater. Chem. A. 8 (2020) 14214–14222, https://doi.org/10.1039/d0ta05429a.

[22] M.-H. Cao, Y. Wang, Z. Shadike, J.-L. Yue, E. Hu, S.-M. Bak, Y.-N. Zhou, X.-Q. Yang, Z.-W. Fu, Suppressing the chromium disproportionation reaction in O3-type layered cathode materials for high capacity sodium-ion batteries, J. Mater. Chem. A. 5 (2017) 5442–5448, https://doi.org/10.1039/C6TA10818K.

[23] Y. Wang, G. Hu, Z. Peng, Y. Cao, X. Lai, X. Qi, Z. Gan, W. Li, Z. Luo, K. Du, Influence of Li substitution on the structure and electrochemical performance of P2-type $Na_{0.67}Ni_{0.2}Fe_{0.15}Mn_{0.65}O_2$ cathode materials for sodium ion batteries, J. Power Sources. 396 (2018) 639–647, https://doi.org/10.1016/j.jpowsour.2018.06.058.

[24] Y.M. Zheng, X.B. Huang, X.M. Meng, S.D. Xu, L. Chen, S. Bin Liu, D. Zhang, Copper and Zirconium Codoped O3-Type Sodium Iron and Manganese Oxide as the Cobalt/Nickel-Free High-Capacity and Air-Stable Cathode for Sodium-Ion Batteries, ACS Appl, Mater. Interfaces. 13 (2021) 45528–45537, https://doi.org/10.1021/acsami.1c12684.

[25] L. Zhang, T. Yuan, L. Soule, H. Sun, Y. Pang, J. Yang, S. Zheng, Enhanced Ionic Transport and Structural Stability of Nb-Doped O3-$NaFe_{0.55}Mn_{0.45-x}Nb_xO_2$ Cathode Material for Long-Lasting Sodium-Ion Batteries, ACS Appl, Energy Mater. 3 (2020) 3770–3778, https://doi.org/10.1021/acsaem.0c00238.

[26] D. Darbar, N. Muralidharan, R.P. Hermann, J. Nanda, I. Bhattacharya, Evaluation of electrochemical performance and redox activity of Fe in Ti doped layered P2-$Na_{0.67}Mn_{0.5}Fe_{0.5}O_2$ cathode for sodium ion batteries, Electrochim. Acta. 380 (2021) 138156.

[27] Z. Chen, M. Yang, G. Chen, G. Tang, Z. Huang, M. Chu, R. Qi, S. Li, R. Wang, C. Wang, T. Zhang, J. Zhai, W. Zhao, J. Zhang, J. Chen, L. He, J. Xu, W. Yin, J. Wang, Y. Xiao, Triggering anionic redox activity in Fe/Mn-based layered oxide for high-performance sodium-ion batteries, Nano Energy. 94 (2022), 106958, https://doi.org/10.1016/j.nanoen.2022.106958.

[28] Y. Lee, H. Park, M. Cho, J. Ahn, W. Ko, J. Kang, Y.J. Choi, H. Kim, I. Park, W. Ryu, J. Hong, J. Kim, Li-Rich Mn–Mg Layered Oxide as a Novel Ni-/Co-Free Cathode, Adv. Funct. Mater. 2204354 (2022) 2204354, https://doi.org/10.1002/adfm.202204354.

[29] Q.C. Wang, J.K. Meng, X.Y. Yue, Q.Q. Qiu, Y. Song, X.J. Wu, Z.W. Fu, Y.Y. Xia, Z. Shadike, J. Wu, X.Q. Yang, Y.N. Zhou, Tuning P2-Structured Cathode Material by Na-Site Mg Substitution for Na-Ion Batteries, J. Am. Chem. Soc. 141 (2019) 840–848, https://doi.org/10.1021/jacs.8b08638.

[30] J. Rodríguez-Carvajal, Recent advances in magnetic structure determination by neutron powder diffraction, Phys. B Condens. Matter. 192 (1993) 55–69, https://doi.org/10.1016/0921-4526(93)90108-I.

[31] B. Ravel, M. Newville, ATHENA and ARTEMIS: Interactive graphical data analysis using IFEFFIT, Phys. Scr. T. T 115 (2005) 1007–1010, https://doi.org/10.1238/Physica.Topical.115a01007.

[32] G. Kresse, J. Furthmüller, Efficiency of ab-initio total energy calculations for metals and semiconductors using a plane-wave basis set, Comput. Mater. Sci. 6 (1996) 15–50, https://doi.org/10.1016/0927-0256(96)00008-0.

[33] P.E. Blöchl, Projector augmented-wave method, Phys. Rev. B. 50 (1994) 17953–17979, https://doi.org/10.1103/PhysRevB.50.17953.

[34] J.P. Perdew, K. Burke, M. Ernzerhof, Generalized Gradient Approximation Made Simple, Phys. Rev. Lett. 77 (1996) 3865–3868, https://doi.org/10.1103/PhysRevLett.77.3865.

[35] G. Sai Gautam, E.A. Carter, Evaluating transition metal oxides within DFT-SCAN and SCAN+U frameworks for solar thermochemical applications, Phys. Rev. Mater. 2 (2018) 1–30, https://doi.org/10.1103/PhysRevMaterials.2.095401.

[36] A. Jain, G. Hautier, S.P. Ong, C.J. Moore, C.C. Fischer, K.A. Persson, G. Ceder, Formation enthalpies by mixing GGA and GGA + U calculations, Phys. Rev. B - Condens. Matter Mater. Phys. 84 (2011) 1–10, https://doi.org/10.1103/PhysRevB.84.045115.

[37] J. Heyd, G.E. Scuseria, M. Ernzerhof, Erratum: Hybrid functionals based on a screened Coulomb potential (Journal of Chemical Physics (2003) 118 (8207)), J. Chem. Phys. 124 (2006), https://doi.org/10.1063/1.2204597.

[38] A. Van der Ven, J.C. Thomas, Q. Xu, J. Bhattacharya, Linking the electronic structure of solids to their thermodynamic and kinetic properties, Math. Comput. Simul. 80 (2010) 1393–1410, https://doi.org/10.1016/j.matcom.2009.08.008.

[39] G. Henkelman, B.P. Uberuaga, H. Jónsson, A climbing image nudged elastic band method for finding saddle points and minimum energy paths, J. Chem. Phys. 113 (2000) 9901–9904, https://doi.org/10.1063/1.1329672.

[40] G. Henkelman, H. Jónsson, Improved tangent estimate in the nudged elastic band method for finding minimum energy paths and saddle points, J. Chem. Phys. 113 (2000) 9978–9985, https://doi.org/10.1063/1.1323224.

[41] Y. Huang, Y. Zhu, A. Nie, H. Fu, Z. Hu, X. Sun, S. Haw, J. Chen, T. Chan, S. Yu, G. Sun, G. Jiang, J. Han, W. Luo, Y. Huang, Enabling Anionic Redox Stability of P2-$Na_{5/6}Li_{1/4}Mn_{3/4}O_2$ by Mg Substitution, Adv. Mater. 34 (2022) 2105404, https://doi.org/10.1002/adma.202105404.

[42] R.J. Clément, J. Billaud, A. Robert Armstrong, G. Singh, T. Rojo, P.G. Bruce, C. P. Grey, Structurally stable Mg-doped P2-$Na_{2/3}Mn_{1-y}Mg_yO_2$ sodium-ion battery cathodes with high rate performance: insights from electrochemical, NMR and diffraction studies, Energy Environ. Sci. 9 (2016) 3240–3251, https://doi.org/10.1039/C6EE01750A.

[43] J.M. Paulsen, R.A. Donaberger, J.R. Dahn, Layered T2-, O6-, O2-, and P2-Type $A_{2/3}[M'^{2+}_{1/3}M^{4+}_{2/3}]O_2$ Bronzes, A = Li, Na; M' = Ni, Mg; M = Mn, Ti, Chem. Mater. 12 (2000) 2257–2267, https://doi.org/10.1021/cm990810d.

[44] U. Maitra, R.A. House, J.W. Somerville, N. Tapia-Ruiz, J.G. Lozano, N. Guerrini, R. Hao, K. Luo, L. Jin, M.A. Pérez-Osorio, F. Massel, D.M. Pickup, S. Ramos, X. Lu, D.E. McNally, A.V. Chadwick, F. Giustino, T. Schmitt, L.C. Duda, M.R. Roberts, P. G. Bruce, Oxygen redox chemistry without excess alkali-metal ions in $Na_{2/3}[Mg_{0.28}Mn_{0.72}]O_2$, Nat. Chem. 10 (2018) 288–295, https://doi.org/10.1038/nchem.2923.

[45] F. Li, K. Fan, P. Hou, H. Huang, Boosting the Redox Kinetics of High-Voltage P2-Type Cathode by Radially Oriented 010 Exposed Nanoplates for High-Power Sodium-Ion Batteries, Small Struct. 3 (2022) 2100123, https://doi.org/10.1002/sstr.202100123.

[46] P.F. Wang, H.R. Yao, X.Y. Liu, Y.X. Yin, J.N. Zhang, Y. Wen, X. Yu, L. Gu, Y.G. Guo, Na^+/vacancy disordering promises high-rate Na-ion batteries, Sci. Adv. 4 (2018) 1–10, https://doi.org/10.1126/sciadv.aar6018.

[47] K. Luo, M.R. Roberts, R. Hao, N. Guerrini, D.M. Pickup, Y.-S. Liu, K. Edström, J. Guo, A.V. Chadwick, L.C. Duda, P.G. Bruce, Charge-compensation in 3d-transition-metal-oxide intercalation cathodes through the generation of localized electron holes on oxygen, Nat. Chem. 8 (2016) 684–691, https://doi.org/10.1038/nchem.2471.

[48] H. Lee, S.B. Lim, J.Y. Kim, M. Jeong, Y.J. Park, W.-S. Yoon, Characterization and Control of Irreversible Reaction in Li-Rich Cathode during the Initial Charge Process, ACS Appl. Mater. Interfaces. 10 (2018) 10804–10818, https://doi.org/10.1021/acsami.7b12722.

[49] G. Assat, A. Iadecola, D. Foix, R. Dedryvere, J.M. Tarascon, Direct Quantification of Anionic Redox over Long Cycling of Li-Rich NMC via Hard X-ray Photoemission Spectroscopy, ACS Energy Lett. 3 (2018) 2721–2728, https://doi.org/10.1021/acsenergylett.8b01798.

[50] J. Ahn, J. Kang, M.-K. Cho, H. Park, W. Ko, Y. Lee, H.-S. Kim, Y.H. Jung, T.-Y. Jeon, H. Kim, W.-H. Ryu, J. Hong, J. Kim, Selective Anionic Redox and Suppressed Structural Disordering Enabling High-Energy and Long-Life Li-Rich Layered-Oxide Cathode, Adv. Energy Mater. 11 (47) (2021) 2102311.

[51] S. Roychoudhury, R. Qiao, Z. Zhuo, Q. Li, Y. Lyu, J.H. Kim, J. Liu, E. Lee, B. J. Polzin, J. Guo, S. Yan, Y. Hu, H. Li, D. Prendergast, W. Yang, Deciphering the Oxygen Absorption Pre-edge: A Caveat on its Application for Probing Oxygen Redox Reactions in Batteries, Energy Environ. Mater. 4 (2021) 246–254, https://doi.org/10.1002/eem2.12119.

[52] M. Sathiya, G. Rousse, K. Ramesha, C.P. Laisa, H. Vezin, M.T. Sougrati, M.-L. Doublet, D. Foix, D. Gonbeau, W. Walker, A.S. Prakash, M. Ben Hassine, L. Dupont, J.-M. Tarascon, Reversible anionic redox chemistry in high-capacity layered-oxide electrodes, Nat. Mater. 12 (2013) 827–835, https://doi.org/10.1038/nmat3699.

[53] M.-H. Cao, R.-Y. Li, S.-Y. Lin, S.-D. Zheng, L. Ma, S. Tan, E. Hu, Z. Shadike, X.-Q. Yang, Z.-W. Fu, Oxygen redox chemistry in P2-$Na_{0.6}Li_{0.11}Fe_{0.27}Mn_{0.62}O_2$ cathode for high-energy Na-ion batteries, J. Mater. Chem. A. 9 (2021) 27651–27659, https://doi.org/10.1039/D1TA08471B.

[54] X. Rong, J. Liu, E. Hu, Y. Liu, Y. Wang, J. Wu, X. Yu, K. Page, Y.-S. Hu, W. Yang, H. Li, X.-Q. Yang, L. Chen, X. Huang, Structure-Induced Reversible Anionic Redox Activity in Na Layered Oxide Cathode, Joule. 2 (2018) 125–140, https://doi.org/10.1016/j.joule.2017.10.008.

[55] X. Cao, H. Li, Y. Qiao, X. Li, M. Jia, J. Cabana, H. Zhou, Stabilizing Reversible Oxygen Redox Chemistry in Layered Oxides for Sodium-Ion Batteries, Adv. Energy Mater. 10 (2020) 1–7, https://doi.org/10.1002/aenm.201903785.
[56] Y. Liu, Y. Ying, L. Fei, Y. Liu, Q. Hu, G. Zhang, S.Y. Pang, W. Lu, C.L. Mak, X. Luo, L. Zhou, M. Wei, H. Huang, Valence Engineering via Selective Atomic Substitution on Tetrahedral Sites in Spinel Oxide for Highly Enhanced Oxygen Evolution Catalysis, J. Am. Chem. Soc. 141 (2020) 8136–8145, https://doi.org/10.1021/jacs.8b13701.
[57] R.A. House, G.J. Rees, M.A. Pérez-Osorio, J.J. Marie, E. Boivin, A.W. Robertson, A. Nag, M. Garcia-Fernandez, K.J. Zhou, P.G. Bruce, First-cycle voltage hysteresis in Li-rich 3*d* cathodes associated with molecular O_2 trapped in the bulk, Nat. Energy. 5 (2020) 777–785, https://doi.org/10.1038/s41560-020-00697-2.
[58] R.A. House, J.J. Marie, M.A. Pérez-Osorio, G.J. Rees, E. Boivin, P.G. Bruce, The role of O_2 in O-redox cathodes for Li-ion batteries, Nat. Energy. 6 (2021) 781–789, https://doi.org/10.1038/s41560-021-00780-2.
[59] S. Koo, I.H. Ko, J. Lee, S.M. Kang, S.H. Yu, D. Kim, Unlocking the Intrinsic Origin of the Reversible Oxygen Redox Reaction in Sodium-Based Layered Oxides, ChemElectroChem. 8 (2021) 1464–1472, https://doi.org/10.1002/celc.202100084.
[60] R.A. House, U. Maitra, M.A. Pérez-Osorio, J.G. Lozano, L. Jin, J.W. Somerville, L. C. Duda, A. Nag, A. Walters, K.J. Zhou, M.R. Roberts, P.G. Bruce, Superstructure control of first-cycle voltage hysteresis in oxygen-redox cathodes, Nature. 577 (2020) 502–508, https://doi.org/10.1038/s41586-019-1854-3.
[61] M.M. Rahman, F. Lin, Oxygen Redox Chemistry in Rechargeable Li-Ion and Na-Ion Batteries, Matter. 4 (2021) 490–527, https://doi.org/10.1016/j.matt.2020.12.004.
[62] S. Wu, W. Wang, M. Li, L. Cao, F. Lyu, M. Yang, Z. Wang, Y. Shi, B. Nan, S. Yu, Z. Sun, Y. Liu, Z. Lu, Highly durable organic electrode for sodium-ion batteries via a stabilized α-C radical intermediate, Nat. Commun. 7 (2016) 1–11, https://doi.org/10.1038/ncomms13318.
[63] M. Guignard, C. Didier, J. Darriet, P. Bordet, E. Elkaïm, C. Delmas, P2-Na_xVO_2 system as electrodes for batteries and electron-correlated materials, Nat. Mater. 12 (2013) 74–80, https://doi.org/10.1038/nmat3478.
[64] E. Talaie, V. Duffort, H.L. Smith, B. Fultz, L.F. Nazar, Structure of the high voltage phase of layered P2-$Na_{2/3-z}[Mn_{1/2}Fe_{1/2}]O_2$ and the positive effect of Ni substitution on its stability, Energy Environ. Sci. 8 (2015) 2512–2523, https://doi.org/10.1039/c5ee01365h.
[65] P.F. Wang, Y. You, Y.X. Yin, Y.S. Wang, L.J. Wan, L. Gu, Y.G. Guo, Suppressing the P2–O2 Phase Transition of $Na_{0.67}Mn_{0.67}Ni_{0.33}O_2$by Magnesium Substitution for Improved Sodium-Ion Batteries, Angew. Chemie - Int. Ed. 55 (2016) 7445–7449, https://doi.org/10.1002/anie.201602202.
[66] G. Singh, N. Tapia-Ruiz, J.M. Lopez Del Amo, U. Maitra, J.W. Somerville, A. R. Armstrong, J. Martinez De Ilarduya, T. Rojo, P.G. Bruce, High Voltage Mg-Doped $Na_{0.67}Ni_{0.3-x}Mg_xMn_{0.7}O_2$ (x = 0.05, 0.1) Na-Ion Cathodes with Enhanced Stability and Rate Capability, Chem. Mater. 28 (2016) 5087–5094, https://doi.org/10.1021/acs.chemmater.6b01935.
[67] G. Singh, J.M. López Del Amo, M. Galceran, S. Pérez-Villar, T. Rojo, Structural evolution during sodium deintercalation/intercalation in $Na_{2/3}[Fe_{1/2}Mn_{1/2}]O_2$, J. Mater. Chem. A. 3 (2015) 6954–6961, https://doi.org/10.1039/c4ta06360k.
[68] H. Liu, W. Deng, X. Gao, J. Chen, S. Yin, L. Yang, G. Zou, H. Hou, X. Ji, Manganese-based layered oxide cathodes for sodium ion batteries, Nano Sel. 1 (2020) 200–225, https://doi.org/10.1002/nano.202000030.
[69] N. Yabuuchi, M. Kajiyama, J. Iwatate, H. Nishikawa, S. Hitomi, R. Okuyama, R. Usui, Y. Yamada, S. Komaba, P2-type $Na_x[Fe_{1/2}Mn_{1/2}]O_2$ made from earth-abundant elements for rechargeable Na batteries, Nat. Mater. 11 (2012) 512–517, https://doi.org/10.1038/nmat3309.